Numerical Simulations of Conditionally Unstable Flows over a Mountain Ridge

MARIO MARCELLO MIGLIETTA

Institute of Atmospheric Sciences and Climate (ISAC), Italian National Research Council (CNR), Lecce/Padua, Italy

RICHARD ROTUNNO

NCAR, Boulder, Colorado*

(Manuscript received 28 July 2008, in final form 23 October 2008)

ABSTRACT

Numerical simulations of conditionally unstable flows impinging on a mesoscale mountain ridge have been performed with an explicitly resolving cloud model to investigate the statistically stationary features of the solution precipitation characteristics. The simulations are performed on a three-dimensional domain and at high resolution (grid spacing: 250 m) to properly resolve cellular-scale features. Although the environmental conditions are specified by a simplified idealized conditionally unstable sounding, there are still quite a few external parameters, so only a limited portion of the parameter space was explored. Numerical solutions were first carried out for different uniform-wind profiles impinging on a bell-shaped ridge 2000 m high. In the experiments with weaker environmental wind speeds (2.5 m s^{-1}), the cold-air outflow, caused by the evaporative cooling of rain from precipitating convective cells, is the main mechanism for cell redevelopment and movement; this outflow produces new convective cells near the head of the up- and downstream density currents, which rapidly propagate far from the ridge so that no rainfall is produced close to the ridge at later times. For larger wind speeds (10 and 20 m s^{-1}), there is less time for upwind, evaporation-induced cold-pool formation before air parcels reach the ridge top and descend downwind. For the intermediate wind speed (10 m s^{-1}), evaporation is effective in generating a cold pool only on the downstream side of the ridge, in a region where the air is unsaturated and slow moving. Further experiments with different ridge heights and half-widths were carried out in order to analyze their effect on the distribution and intensity of precipitation. Dimensional analysis reveals that the maximum (nondimensional) rainfall rate mainly depends on the ratio of mountain height to the level of free convection, the ridge aspect ratio, and a parameter that measures the ratio of advective to convective time scales.

1. Introduction

Orographic precipitation in a conditionally unstable atmosphere presents a significant challenge to the analyst/forecaster. In comparison with a stably stratified atmosphere, in which orographic lifting provides the main impetus to ridge-scale condensation and precipitation, lifting of conditionally unstable air initiates a group of convective-scale updrafts and downdrafts that act in concert to produce precipitation (Smith 1979, p. 175). This group of precipitating, interacting, three-dimensional, time-dependent cloud cells may be considered a class of turbulent flow (Bryan et al. 2003), so the statistical nature of the problem is unavoidable (e.g., Walser et al. 2004). In the present study, we report on a series of three-dimensional numerical simulations of conditionally unstable flow past a mountain ridge and attempt to characterize the response of the along-ridge-averaged precipitation to variations in the upstream (conditionally unstable) thermodynamic sounding, mean wind, and topography.

Experience shows (e.g., Richard et al. 2007), and the present simulations reaffirm, that with deep orographic convection important aspects of the modeled precipitation are very sensitive to a number of factors. Within the context of a two-dimensional ridge, consider for example the factors that might determine the location of the most intense rainfall. On one hand, the initial triggering of cells

* The National Center for Atmospheric Research is sponsored by the National Science Foundation.

Corresponding author address: Mario Marcello Miglietta, CNR-ISAC, Strada Provinciale Lecce-Monteroni, Km 1.200, 73100 Lecce, Italy.
E-mail: m.miglietta@isac.cnr.it

DOI: 10.1175/2009JAS2902.1

upstream of the ridge top may be fairly easy to predict given knowledge of the level of free convection (LFC) and the orographic uplift; on the other hand, after formation a cell may move according to the winds aloft and thus produce rain at another location and, along with it, cool outflows that may produce other cells at yet other locations, and so on.

The potentially most dangerous cases are those in which deep convective cells continually precipitate in more or less the same location with respect to the mountain topography. The occurrence of such cases (which often produce flash flooding) around the world is well documented in the literature (Schroeder 1977; Caracena et al. 1979; Sénési et al. 1996; Pontrelli et al. 1999; Romero et al. 2000). Although the common ingredient for these cases is the low-level flow of a conditional unstable air mass toward orography, it is not generally sufficient since, as noted above, one can envision scenarios in which deep convective cells do not concentrate their precipitation in the same location. Hence, it is the goal of the present research to ascertain the factors that produce intense orographic precipitation within the context of a simple but nontrivial meteorological model.

Although the literature includes many observational analyses of orographic convective precipitation, numerical idealized studies of deep convection in mountainous regions are relatively few and challenging owing to the large number of control parameters (i.e., properties of the upstream wind and temperature profiles, the shape of the mountain, etc.). For example, the devastating Big Thompson storm (Caracena et al. 1979) was studied using idealized two- and three-dimensional numerical cloud model simulations (Yoshizaki and Ogura 1988). Such experiments were able to reproduce the observed storm in many aspects, although with some differences between the 2D and 3D simulations. An interesting finding was the existence of a cold pool beneath the storm in a situation where the cloud base height was lower than the mountain height: their model results show the storm slanted vertically so that precipitating particles fell through the cloud-free layer, thus enhancing evaporative cooling. However, from limited case-specific simulations, it is difficult to generalize these results.

In an attempt to study the problem from a more generic viewpoint, Chu and Lin (2000, hereafter CL2000) performed two-dimensional numerical simulations of uniform flow of a conditionally unstable air mass past a 2D ridge. They identified three distinct flow regimes as a function of the Froude number (defined as $F = U/Nh_m$, where U is the basic-state wind speed, N the dry Brunt–Väisälä frequency, and h_m the maximum ridge height): in regime I (small F), a density current and a convective system propagate upstream of the ridge; in regime II (intermediate F), the propagation speed of the density current is approximately balanced by the basic-state wind so that the stationary density current and convective system remain close to the ridge; in regime III (large F), the density current is swept downstream by the relatively strong wind, leading to large precipitation accumulations on the peak or slightly upslope. Further results were reported in Chen and Lin (2005) (again using a 2D model but with horizontal grid size = 1 km instead of the 2.5 km used in CL2000) where a 2D moist-flow regime diagram, based on F and the convective available potential energy (CAPE), was proposed; also, a fourth flow regime, characterized by orographic stratiform precipitation system over the ridge and a leeside downstream-propagating convective system, was identified.[1]

As mentioned above, a group of precipitating updrafts and downdrafts is a class of turbulent flows. Therefore a more realistic model of orographic convection should have the capability of resolving the three-dimensional structure of, and interactions among, the convective elements (as the large eddies), as demonstrated in Bryan et al. (2003). In the present study we report on 3D simulations of conditionally unstable flow over a 2D ridge; analysis of the along-ridge-averaged properties is therefore based on a more realistic (than the 2D) version of the convective cells and their mutual interactions in response to orographic forcing. In section 2, the model domain and resolution that make the present large-eddy simulation (LES) of orographic convection feasible are described, along with the initial conditions that delineate the parameter space for the present study. The results concerning the intensity and distribution of the precipitation are described and analyzed in sections 3 and 4, respectively. Concluding remarks and the prospects for future work are given in section 5.

2. Numerical experiments

The present study was carried out using the 3D numerical model described in Bryan and Fritsch (2002) (http://www.mmm.ucar.edu/people/bryan/cm1), which was designed with particular emphasis on cloud-scale motions and processes. To solve the nonhydrostatic, compressible equations for momentum, mass, energy, and water substance, a split-time-step technique is used to maintain the stability of the acoustic modes (Klemp and Wilhelmson 1978), with an explicit calculation of the acoustic terms in the horizontal, and a vertical implicit

[1] We note that, since neither N nor h_m was varied in these experiments, the above-reported variations of the solution with the nondimensional parameter F should be interpreted simply as variations with the dimensional parameter U. For further comments, see section 3b.

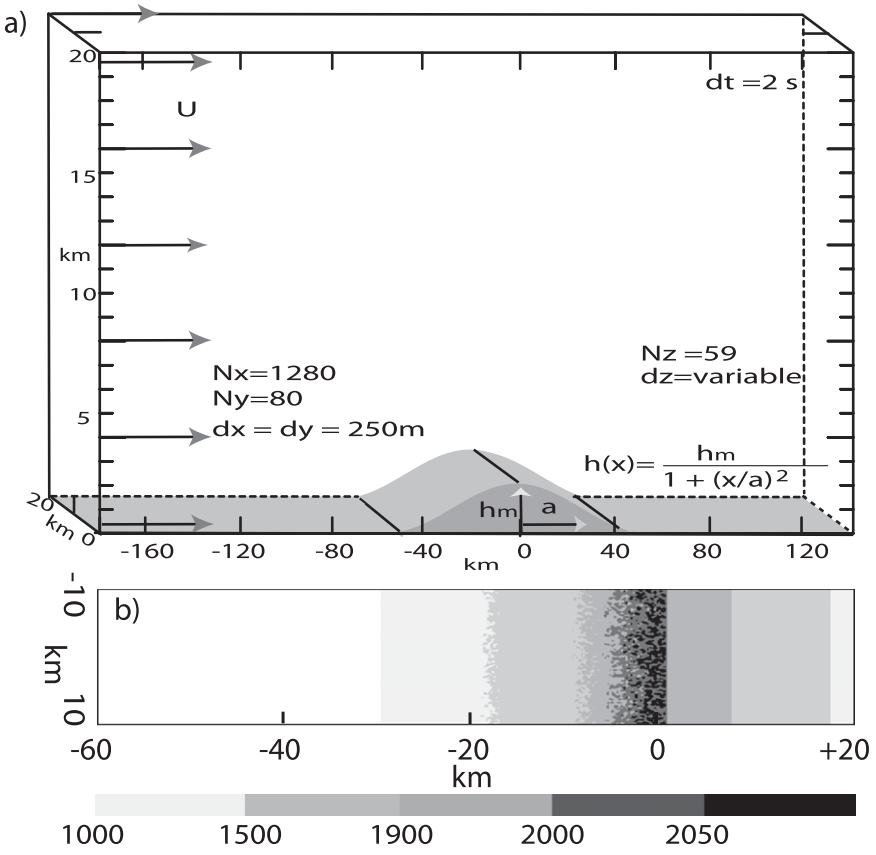

FIG. 1. (a) Numerical setup and (b) terrain profile of the experiments. In (a) N_x, N_y, and N_z are, respectively, the number of grid points in x and y directions and the number of vertical levels. In (b) the terrain profile is shown in an expanded view close to the mountain top.

solver. Integration of variables on the larger time step is performed using the Runge–Kutta technique formulated for compressible models by Wicker and Skamarock (2002). A sixth-order advection scheme is chosen in the horizontal, with sixth-order artificial diffusion applied to all variables; a fifth-order scheme is chosen in the vertical with no artificial diffusion.

Subgrid-scale turbulence is parameterized using a turbulent kinetic energy closure (Deardorff 1980). Microphysical processes are parameterized through the Lin et al. (1983) scheme with modifications by the Goddard modeling group (Braun and Tao 2000). The scheme includes ice; graupel is defined as a large-ice category (no hail is included). In the present experiments the earth's rotation is neglected.

The lower boundary is free-slip, while a Rayleigh-damping layer is applied to the uppermost 6 km, serving to absorb vertically propagating waves. The total outward mass flux (through the open boundaries; see below) is not allowed to exceed the total inward mass flux; this constraint helps to prevent a runaway outward flux that can cause a domain-total mass loss and pressure fall.

a. Model domain and resolution

The numerical setup employed in the present experiments is shown in Fig. 1a. Although the basic geometry of the ridge is two-dimensional, the physics of precipitating convection is three-dimensional—hence the need for a three-dimensional domain. To carry out computations at reasonable cost, but without significant sacrifice of physical realism, we arrived at the following compromise: the domain has to be long enough to contain the significant features of the solution for the chosen integration time; in the present case, a domain length of approximately 320 km (in the along-flow or x direction) was sufficient. The domain also has to be wide enough to contain the largest along-ridge scales that might appear in the solution; through a process of trial and error,[2] a 20-km width (in the across-flow or y direction) was found to be adequate. For the chosen thermodynamic

[2] The 20-km domain was determined by carrying out solutions for a smaller domain width and then increasing it until no substantial changes were observed in the solutions.

sounding (see below), a domain height of 20 km (in the vertical or z direction) was selected. Although marginally acceptable for simulating 3D precipitating turbulent convection (see below), we set the horizontal grid spacings $dx = dy = 250$ m; the vertical grid spacing $dz = 250$ m for $z < 9000$ m, increases to $dz = 500$ m from $z = 9000$ to 10 500 m, and then remains constant at $dz = 500$ m up to the top of the domain. The horizontal extent of the domain was chosen as a compromise between the need to limit the computational cost and the requirement to minimize the potentially spurious effects of gravity wave reflection at the inflow and outflow boundaries, where an open (wave radiation) condition (Durran and Klemp 1983) is applied. The solution is taken to be periodic in the y direction. Experiments performed with a domain twice as long show that the results reported herein are not dependent on the length of the channel. The time step $dt = 2$ s for all experiments.

The horizontal resolution appropriate for the simulation of deep moist convection with cloud-resolving models has been recently addressed from a turbulence perspective (Bryan et al. 2003). Although a grid spacing of $O(1$ km) is often sufficient to simulate the basic features of deep moist convection, some important details of convection—such as the precipitation distribution and amount—show a strong sensitivity to horizontal resolution as the grid spacing is reduced to less than 1 km. This sensitivity is mainly a consequence of the fact that only by going down to a grid spacing of $O(100$ m) will allow in-cloud turbulence to occur (Droegemeier et al. 1997; Petch et al. 2002). High-resolution simulations can resolve the inertial subrange of turbulence, wherein kinetic energy is transferred from the large-eddy scale (i.e., the thunderstorm scale) to smaller scales (i.e., the subcloud scale), only when the grid spacing is less than about 250 m (although a truly statistically converged, resolution-independent result would require a grid spacing less than 100 m; see Bryan et al. 2003).

Thus, we consider a horizontal resolution of 250 m as adequate for the numerical experiments employed in the present paper. However, some preliminary 2D experiments were performed to test the solution sensitivity to horizontal resolution in our numerical setup. Two-dimensional simulations using the same external parameters were performed with grid spacings of 250 m, 500 m, and 2500 m, respectively. Our experiments with horizontal grid spacing of 2500 m used in the control experiments of CL2000 are able to reproduce the flow features discussed in that paper (not shown). However, moving from coarse resolution (2500 m) to finer horizontal resolutions (500 and 250 m) in 2D experiments, both quantitative and qualitative differences emerge (although the cases using $dx = dy = 500$ m and those using $dx = dy = 250$ m are qualitatively similar).

b. Environmental conditions

For simplicity, the orography is prescribed by the bell shape

$$h(x) = h_m/\{1 + [(x - x_0)/a]^2\}, \quad (1)$$

with a representing the ridge half-width; a bird's-eye view of the orography is shown in Fig. 1a. The peak of the ridge is positioned at x_0, which is located 20 km downstream of the center of the domain; this configuration is chosen so as to increase the distance of the ridge from the inflow boundary, where gravity waves could be reflected toward the ridge and thus affect the windward-slope precipitation features in which we are most interested.

To break the y symmetry of the numerical setup and obtain a fully three-dimensional solution, some energy must be projected into the subridge-scale convective motions to initiate isolated convective cells. This small-scale energy is provided in our numerical simulations by adding small-amplitude irregularities to the ridge. These irregularities are created by assigning a uniformly distributed random number (ranging from 0 to 100 m for the higher ridge and from 0 to 50 m for the other cases) to each grid point over the ridge surface from 30 km upstream to the peak, as shown in Fig. 1b. Recent studies (Kirshbaum et al. 2007a,b) have shown that small-scale features of the topography can determine the characteristics of the sometimes-observed banded nature of convection in cases of relatively weak and shallow moist instability. In the present case, only cases of strong and deep moist instability were modeled, so such banded structures over the ridge were not dominant features of the solutions.

The initial conditions are horizontally homogeneous and are defined using the analytic expression for temperature and moisture profiles provided in Fig. 2 (following Weisman and Klemp 1982), but with a vertically uniform atmospheric wind speed perpendicular to the axis of the ridge. This vertical sounding was used in previous studies of idealized orographic flows (CL2000; Reeves and Lin 2007). Some of the most significant features of such a thermodynamic profile are the low LCL [~885 hPa (1.1 km)] and LFC [~830 hPa (1.8 km)], the large CAPE (= 1925 J kg^{-1}), and a fairly well-mixed boundary layer (with a constant mixing ratio). The convective inhibition (CIN) is positive (=12 J kg^{-1}); thus, a small uplift is required to release the large convective instability.

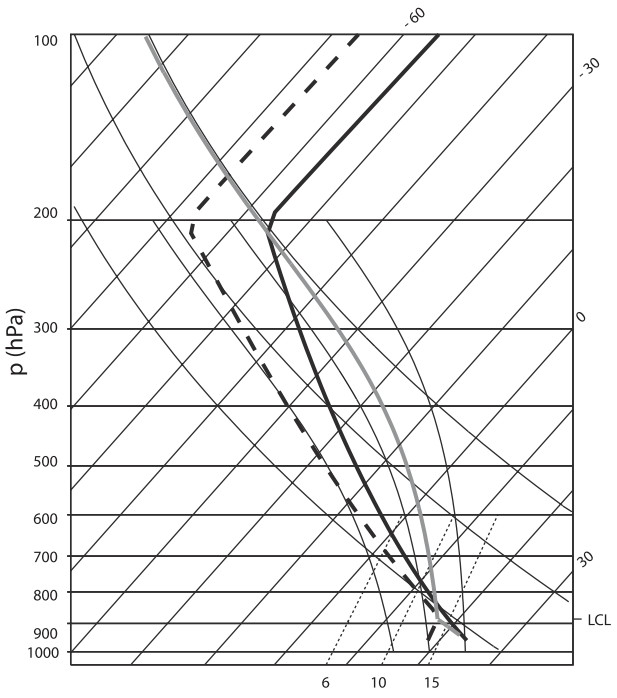

FIG. 2. Idealized profiles of temperature (solid line) and dewpoint (dashed line) used in our experiments (CAPE = 1925 J kg^{-1}). The bold gray line represents the pseudoadiabatic curve of a parcel lifted from the surface.

The mountain ridge is introduced impulsively at time $t = 0$ into an airstream flowing at uniform speed U, which we will vary as an input parameter in the present study. Although the observational evidence suggests that rain accumulation is sensitive to variations of the ambient wind with height (Caracena et al. 1979), for the present initial study, the inclusion of a vertically varying wind was considered too large an expansion of the already large parameter space to be explored and is therefore deferred to future work.

c. Parameter study

The effect of the orography on a conditionally unstable flow in the atmosphere is extremely complex. For example, even with the highly idealized environmental conditions described in the previous subsections, the number of control parameters is large. In fact, for the numerical setup shown in Figs. 1 and 2, even excluding the microphysical parameters (such as the terminal fall velocity of the condensate), which are part of the parameterization scheme and over which there is no external control, at least 10 different control parameters can be identified; eight of them are related to the sounding characteristics—U, N^2, DCAPE (the maximum increase in kinetic energy gained in the downdraft resulting from evaporative cooling; see Gilmore and Wicker 1998), CAPE, CIN, LFC, LCL, and the height of the tropopause h_t; finally, two parameters are required to define the ridge dimensions (h_m, a) in the simple case of a bell-shaped ridge.

Considering that only length and time appear as dimensions in these parameters, dimensional analysis says that eight nondimensional numbers can be identified that can govern the behavior of the solutions. Thus, the solutions may depend on (e.g.)

$$\frac{h_m}{h_t}, \quad \frac{h_m}{a}, \quad \frac{h_m}{\mathrm{LFC}}, \quad \frac{h_m}{\mathrm{LCL}}, \quad \frac{\mathrm{DCAPE}}{U^2}, \quad \frac{\mathrm{CAPE}}{\mathrm{CIN}}, \quad \frac{h_m N}{U}, \quad \frac{\mathrm{CAPE}}{U^2} \tag{2}$$

or, of course, on any other grouping of them. With the computing resources available to us, it was beyond our capability to explore the whole parameter space, so we could not draw general conclusions on the dependence of the solutions on all these parameters.

Based on experience with both convection and orographic flow, we confined our analysis to a limited portion of the parameter space by investigating the sensitivity of the solutions to U, h_m, and a. Although limited, the solution response to variations in these parameters is quite varied, and the categorization of the solution types in terms of nondimensional parameters is nontrivial (see section 4).

The results of these experiments are discussed in section 3. For U, three values have been chosen to represent small ($U = 2.5$ m s^{-1}), intermediate ($U = 10$ m s^{-1}), and large ($U = 20$ m s^{-1}) wind speed. Similarly, three different ridge heights and half-widths have been chosen as representative of low ($h_m = 500$ m), medium ($h_m = 1000$ m), or high ($h_m = 2000$ m) and broader or narrower ($a = 60$, 30, 15 km) ridges. In addition, the effect of very low ridges ($h_m = 100$ m) was tested, but the orographic forcing was too weak to produce a stationary solution in that case. Finally, experiments with different values of CAPE were done; the sounding was modified by changing θ_{tr}, the potential temperature at the tropopause, with respect to the value used in most of the experiments ($\theta_{tr} = 343$ K). In this way, CAPE varies whereas the low-level temperature and humidity profiles, as well as other relevant sounding parameters such as h_t, CIN, LCL, and LFC, change only slightly (however, DCAPE changes significantly).

Other simulations were performed with different values of U, a, and CAPE to fill in certain parts of the parameter space. The complete list of experiments performed is provided in Table 1.

TABLE 1. List of all experiments. The simulations are identified with the value of U (m s^{-1}), h_m (m), a (km), and CAPE (m^2 s^{-2}). The values of R_m (mm h^{-1}), $R_{\rm tot}$ (mm h^{-1}), X_m (km), and figure references are also shown. The values of R_m and $R_{\rm tot}$ are set to zero in case of nonstationary rainfall.

U	h_m	a	CAPE	R_m	R_{tot}	X_m	Figure(s)
20	2000	15	1925	31	24	−6	10a
20	2000	30	480	18	36	−7	
20	2000	30	1250	22	40	0	
20	2000	30	1925	21	39	4	3c, 4c, 5c, 6c, 7c, 10a
20	2000	30	2740	21	34	−23	
20	2000	60	480	10	27	−22	
20	2000	60	1925	20	49	−25	10a
20	2000	120	480	4	12	−39	
20	2000	120	1925	8	24	−30	
20	1000	15	1925	21	8	13	10b
20	1000	30	480	14	22	0	
20	1000	30	1925	19	18	−8	10b
20	1000	60	1925	13	26	−40	10b
20	500	15	1925	0	0		10c
20	500	30	1925	9	6	19	10c
20	500	60	1925	8	11	2	10c
20	100	30	1925	0	0		
15	2000	15	1925	32	19	−7	
15	2000	30	1925	20	28	−31	
15	2000	60	1925	17	34	−25	
10	2000	15	1925	19	31	1	14a
10	2000	30	480	6	13	−5	
10	2000	30	1250	9	20	−11	
10	2000	30	1925	15	25	−18	3b, 4b, 5b, 6b, 7b, 9b, 14a
10	2000	30	2740	19	35	−11	
10	2000	60	1925	12	28	−50	14a
10	1000	7,5	1925	19	19	22	
10	1000	15	1925	19	24	17	14b
10	1000	30	1925	12	22	−4	14b
10	1000	60	1925	12	30	−7	14b
10	500	15	1925	0	0		14c
10	500	30	1925	0	0		14c
10	500	60	1925	0	0		14c
10	100	30	1925	0	0		
5	2000	15	1925	0	0		
5	2000	30	1925	0	0		
5	1000	7,5	1925	0	0		
5	1000	15	1925	0	0		
5	1000	30	1925	0	0		
2,50	2000	15	1925	0	0		
2,50	2000	30	1925	0	0		3a, 4a, 5a, 6a, 7a
2,50	2000	60	1925	0	0		
2,50	1000	15	1925	0	0		
2,50	1000	30	1925	0	0		
2,50	1000	60	1925	0	0		
2,50	500	15	1925	0	0		
2,50	500	30	1925	0	0		9a
2,50	500	60	1925	0	0		

3. Results

a. Basic features of the solutions

First we discuss the effect of wind speed for a fixed ridge (a = 30 km, h_m = 2000 m). Figures 3a–c show the rain rate over the entire simulation domain for experiments with wind speeds of 2.5, 10, and 20 m s^{-1}, respectively. For the weakest wind speed, the rain rate is calculated in the time interval between 4 and 5 h (after which time the cells move out of the domain), whereas in the other two cases it is calculated as the time interval between 9 and 10 h of simulation when the solution has reached a statistically steady state.

These simulations show a strong dependence of the rain rate on the wind speed. For the case with U = 2.5 m s^{-1}, shown in Fig. 3a, no rainfall occurs close to the ridge after several hours of integration, and two maxima (which will be shown to be moving) are in evidence far upstream and downstream. For the intermediate-wind-speed case shown in Fig. 3b, the rainfall is mainly localized on the upwind side of the ridge, approximately from −50 km to +10 km, and a weak maximum occurs at x = +50 km. For the larger-wind-speed case, shown in Fig. 3c, a rainfall peak larger than 20 mm h^{-1} is simulated at or slightly downstream of the ridge top, and the rainfall is mainly confined to the vicinity of the ridge. For both the U = 10 m s^{-1} and U = 20 m s^{-1} cases, a secondary maximum occurs upstream, close to the upwind side of the main area affected by rainfall, and several rainbands are apparent, especially for U = 10 m s^{-1} (where some maxima are elongated in the x direction from about 20 to 5 km upstream).

Figure 4 shows the vertical velocity at z = 3 km, which reveals the presence of three-dimensional convective updrafts and downdrafts associated with the rainfall patterns upstream of the ridge shown in Fig. 3. The cells in all three cases have a Byers and Braham (1949)-type life cycle but with some significant differences in cell structure. For U = 2.5 m s^{-1} (Fig. 4a), the cells are more elongated in the x direction as compared to the other two cases, probably as a consequence of the shear (see Bryan et al. 2007) induced in the low and middle levels by the density current (see below). For larger wind speeds, the cells are more circularly shaped and are more sparsely distributed for U = 10 m s^{-1} (Fig. 4b) than for U = 20 m s^{-1} (Fig. 4c), where the cells are closer together and more aligned in the y direction.

To better understand the behavior of these simulations, potential temperature perturbations, cloud water (liquid plus ice) and rainwater content, and u wind component are shown in Fig. 5 along vertical cross sections extending from the ground up to 10 km in the vertical and for the entire length of the channel in the x

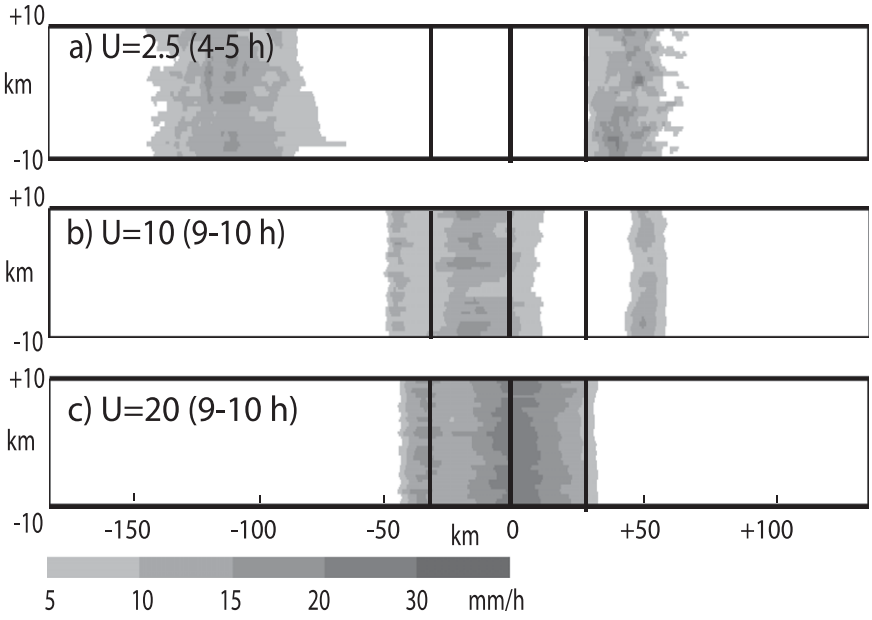

FIG. 3. Rainfall rates simulated in experiments with $a = 30$ km, $h_m = 2000$ m, CAPE = 1925 J kg^{-1}, and U = (a) 2.5 m s^{-1}, (b) 10 m s^{-1}, and (c) 20 m s^{-1}. The rainfall is calculated from $t = 4$ to $t = 5$ h in (a), and from $t = 9$ to $t = 10$ h in (b) and (c). The vertical lines represent the location of the ridge top and of the ridge half-width.

direction. All fields are averaged in the y direction. The results are shown after 5 h for $U = 2.5$ m s^{-1} and at the final integration time $t = 10$ h for the other experiments.

For $U = 2.5$ m s^{-1} (Fig. 5a) a cold pool with a minimum temperature perturbation smaller than -6 K moves toward the entrance of the channel as a density current (as in CL2000's regime I). The solution does not show any upstream blocking at the beginning of the simulation, so the origin and the evolution of the cold pool must be attributed entirely to the moist dynamics; that is, the density current is generated as a consequence of the cooling associated with the evaporation of the rainfall on the upstream side of the ridge. Similar conclusions have been drawn in Stein (2004, p. 497). After approximately 5 h, the cold pool has propagated far upstream and has almost reached the inflow boundary of the domain. The cold-air outflow produces new convective cells on the upstream side of the head of the density current while rainfall is no longer produced close to the ridge. Thus, no stationary solution with rain is found close to the ridge. Experiments with an extended domain in the x direction indicate that the upstream-propagating density current continues in a statistically steady state, producing (and being reinforced by) widely scattered convective cells consistent with the absence of environmental wind shear (Bryan et al. 2006, their Figs. 4–5).

When we consider a larger wind speed ($U = 10$ m s^{-1}, Fig. 5b), convective cells remain quasi stationary over the upwind slope (Fig. 3b). A cold pool on the upstream side of the ridge does not form, even after extending the simulation for a few more hours [this result differs from that found in an analogous experiment performed on a 2D domain where a cold pool was generated upstream (Miglietta and Rotunno 2007)]. On the downstream side, a deep cold pool extends through the end of the domain, with one edge remaining quasi stationary on the downwind side of the ridge. The rainfall responsible for the evaporative cooling is in this case produced by convective cells generated by the convergence between the cold pool and the orographic leeside downslope flow at $x \sim +40$ km. These features correspond to CL2000's regime III. With a further increase of wind speed ($U = 20$ m s^{-1}, Fig. 5c), a downstream convective system (and the associated cold pool) rapidly move out the eastern boundary, advected by the intense downslope flow ($\sim$50 m s^{-1}, which is common in free-slip simulations of downslope wind storms; see, e.g., Durran 1986); quasi-stationary convective cells, deeper and with a water content larger than for the case $U = 10$ m s^{-1}, are simulated on the upstream side of the ridge.

To get a better appreciation of the time-dependent nature of the solutions, the same cases shown in Fig. 5 are displayed in terms of a Hovmöller diagram for the y-averaged rain rate in Fig. 6 (rain rates are evaluated every half hour). For $U = 2.5$ m s^{-1}, Fig. 6a shows the fast ($\sim$10 m s^{-1}) movement of the upstream rainfall toward the inflow boundary of the domain as an effect of the cold-pool propagation; the downstream precipitation

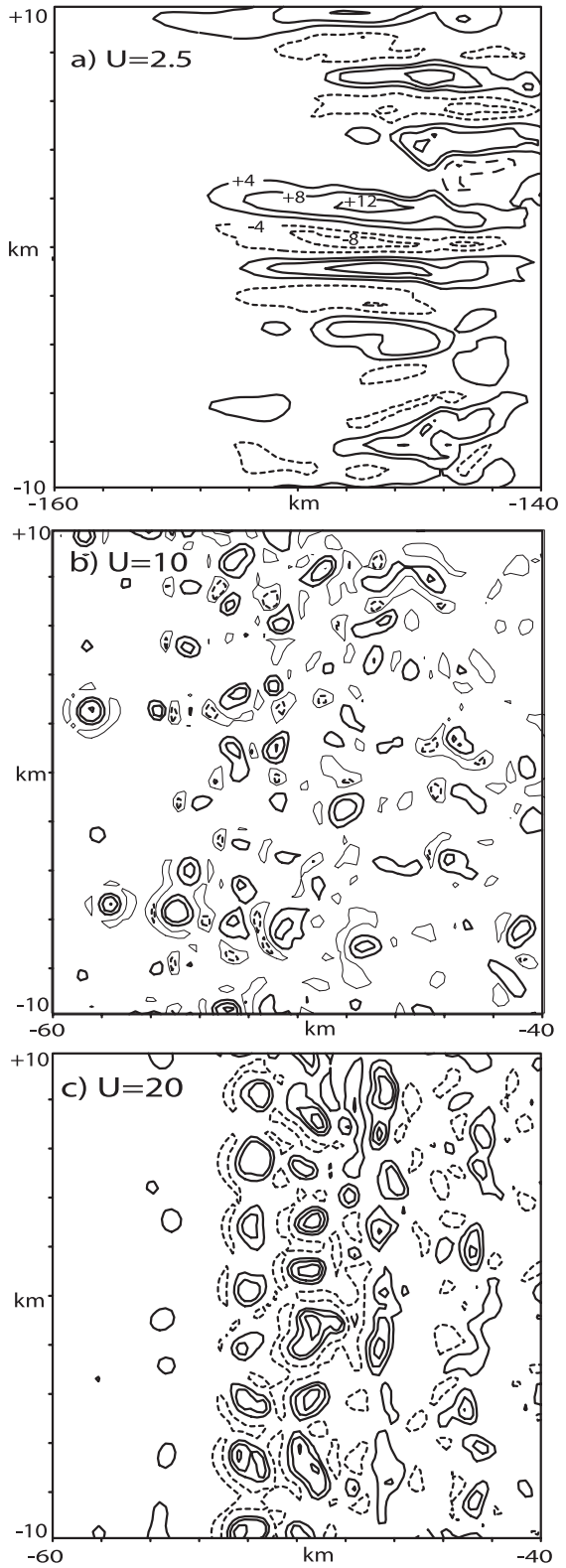

FIG. 4. Vertical velocity at the constant height of 3 km for $U =$ (a) 2.5 m s^{-1}, (b) 10 m s^{-1}, and (c) 20 m s^{-1}. The field is shown at $t = 10$ h, apart from (a), where it is shown after $t = 5$ h. Solid thick lines are used for positive values (contour lines for $w = 4$, 8, 12 m s^{-1}) and dashed lines for negative values (contour lines for $w = -4$, -8 m s^{-1}). A special value of $w = -2$ m s^{-1} is shown in (b) with solid thin lines. The fields are shown in the area where the cells form more upstream.

begins to occur later in the simulation and, thus, after 5 h it still affects a region close to the ridge, although its propagation velocity is similar to that of the upstream density current. For $U = 10$ m s^{-1} (Fig. 6b), the rainfall pattern close to the ridge becomes quasi stationary after about 5 h, while the downstream precipitation, responsible for the cold pool, begins to occur after about 7 h and then remains quasi stationary at about 50 km downstream. For $U = 20$ m s^{-1} (Fig. 6c), the rainfall pattern becomes quasi stationary after a shorter time interval. The presence of convective cells rapidly advected by the intense wind speed toward the outflow boundary is also apparent. This transient feature is reminiscent of the waves generated by the impulsive introduction of the ridge at $t = 0^+$ and can also be observed (although less intense) in the case $U = 10$ m s^{-1} (see the gray area on the right side of Fig. 6b at ~4 h).

From the analysis shown so far, however, it is not clear why convection upwind of the ridge produces no significant cold pool for the larger ambient wind speeds. To help explain the factors influencing cold-air production, we show in Fig. 7 the along-ridge-averaged equivalent potential temperature $\langle\theta_e\rangle$ on a domain corresponding to that of Fig. 5. For the case of the weaker wind speed, Figs. 5a and 7a show that the cold pool is composed of low-θ_e air which, through evaporation of rain, has descended from midlevels to the surface. For the stronger winds, Figs. 7b,c show that the upwind convective cells (Figs. 4b,c) act to vertically mix θ_e such that $\langle\theta_e\rangle$ increases in the midlevels and decreases in the lower levels; note that compared with the weak-wind case there is only a slight reduction of $\langle\theta_e\rangle$ for the upslope flow. It is clear from Fig. 7 that the averaged advective flux of θ_e dominates the vertical flux of the convective cells on the windward slope of the ridge. Alternatively, one can consider that the change in potential temperature θ following a parcel along its mean trajectory can be approximated by $\int dx(C - E)/U$, where C and E are the contribution of condensation and evaporation, respectively. As both C and E associated with the individual cells do not vary significantly (not shown) among the different experiments, the main change in the integral comes from variations in U. For $U = 2.5$ m s^{-1} (Figs. 5a and 7a), the time scale of advection is larger than (or comparable with) the time scale for the formation of cold air through evaporation of rain into midlevel, low-θ_e air with subsequent

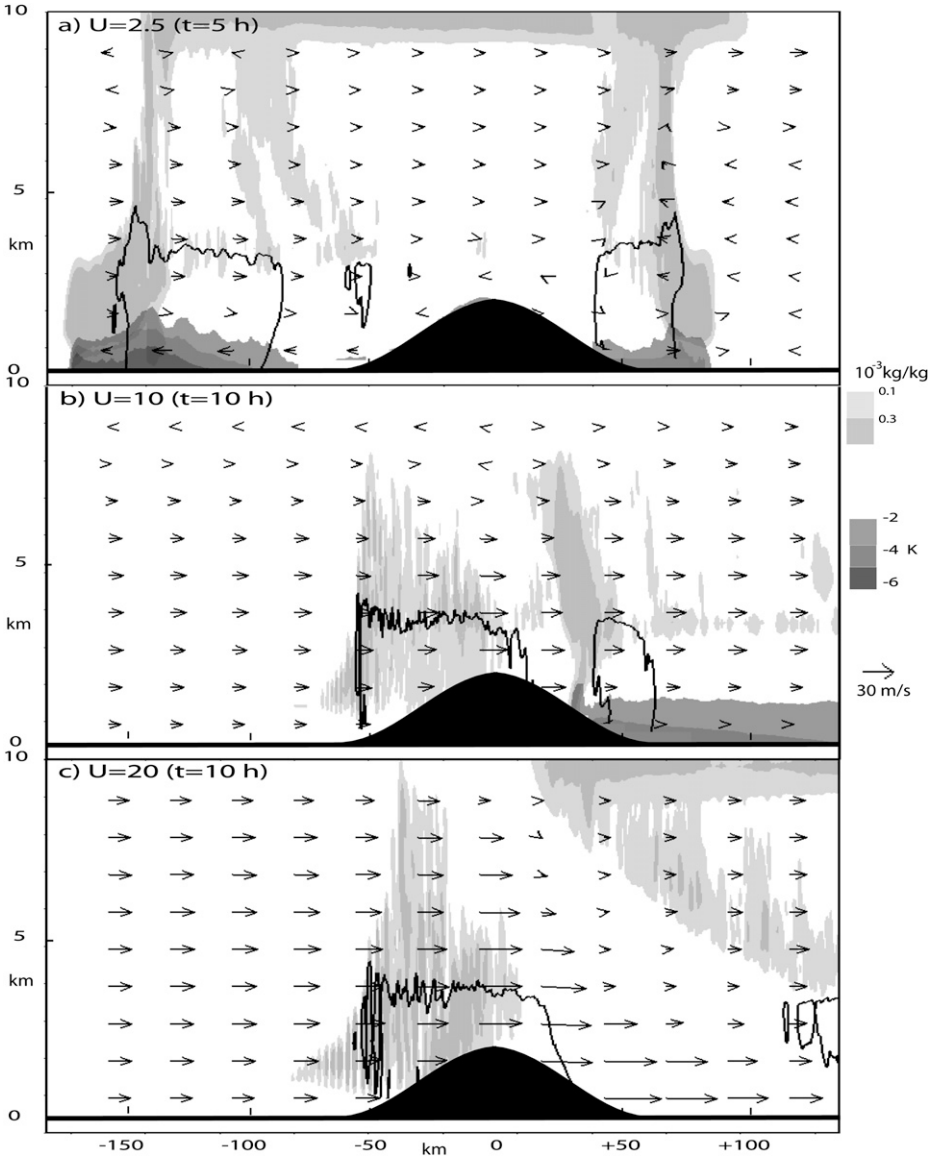

FIG. 5. Vertical cross sections (extending from the ground up to 10 km) of the y average of potential temperature perturbation (dark shaded areas), cloud water plus ice content (light shaded areas), rainwater content (contour line for 0.2×10^{-3} kg kg^{-1}), and wind speed (arrows) for the experiments shown in Fig. 3. The results are shown after $t = 5$ h in (a) and at the final integration time $t = 10$ h in (b) and (c).

descent. For the larger wind speeds, the advective time scale is short and the y-averaged latent heating/cooling of the air mass is dominated by the advection of environmental air with the ambient values of θ. Thus, when U is large, there is no time (from the Lagrangian point of view) for evaporation to have a significant effect on the upstream temperature field.

The mechanisms responsible for the flow features observed in Figs. 5–7 are illustrated in Fig. 8. In the first instance when the ridge is introduced into the flowing airstream, air parcels are lifted. In the above-described experiments, the ridge top is above the level of free convection; therefore the air is forced to flow above the lifting condensation level (~1100 m) and then pass the level of free convection (~1800 m) so that convective cells are triggered. Subsequently, the top panel of Fig. 8 shows that the rainfall generated on the upstream side of the ridge may evaporate into midlevel, potentially cool air, which can descend to the surface and produce a cold outflow. For intermediate to strong wind speeds (middle and lower panels of Fig. 8) the net cooling from evaporation is small compared to the advection of

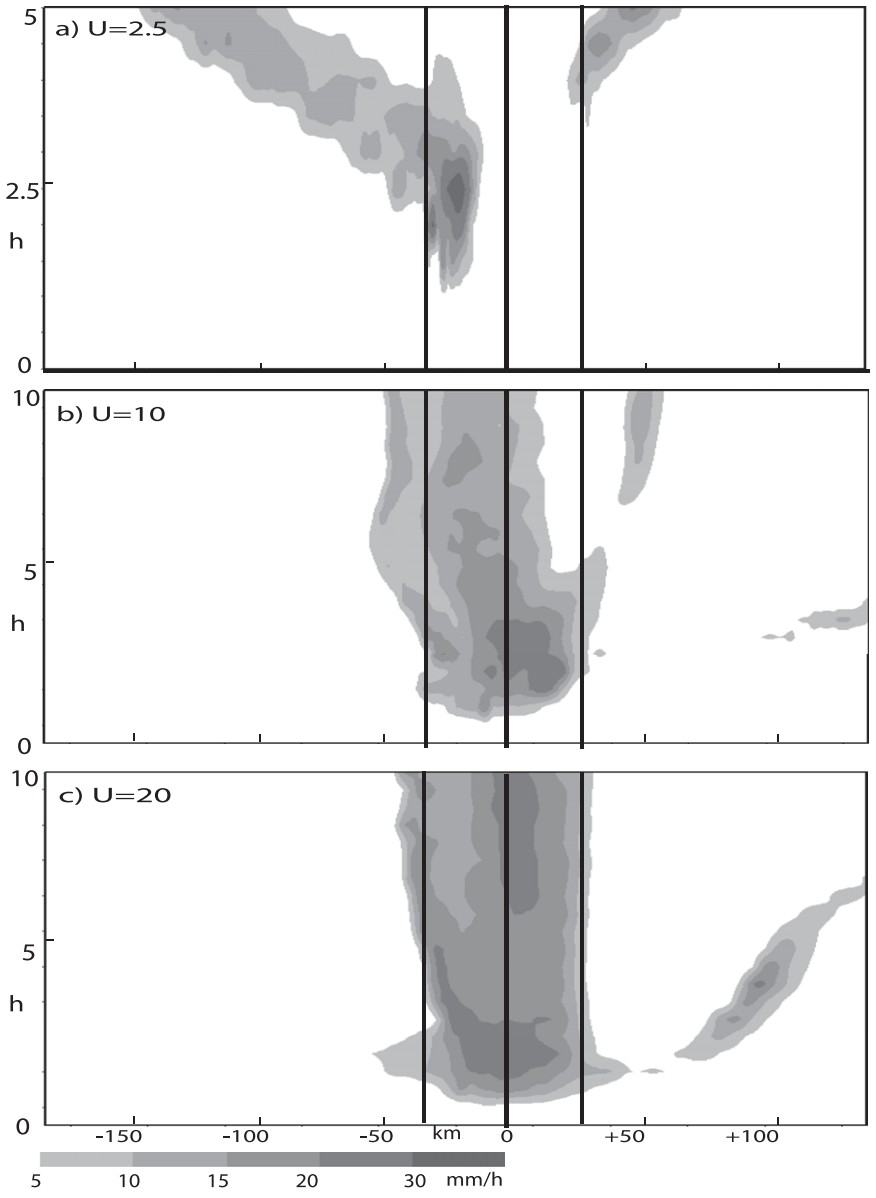

FIG. 6. Hovmöller diagram of the y average of rain rate for the experiments in Fig. 3. The rain rate is calculated every 30 min and is shown from $t = 0$ h to $t = 5$ h in (a) and from $t = 0$ h to $t = 10$ h in (b) and (c).

ambient potential temperature to the windward face of the ridge so that the decrease in potential temperature is minimal. For the intermediate wind case, convection is triggered on the downstream feature of dry windstorm simulations (e.g., Fig. 1b of Durran 1986) loosely termed a ''hydraulic jump''—rain evaporates into the descending low-θ_e air and produces a stationary cold pool.

The relevance of environmental wind speed for the development of density currents has been found in other numerical experiments. Idealized simulations, performed with the atmospheric profiles obtained from the Cagliari sounding during the intensive observing period, IOP 2B, of the Mesoscale Alpine Programme (MAP), but with modified wind speeds, are shown in Stein's (2004) Fig. 5. For large wind speeds, rain evaporation appears not to be active since convective clouds extend close to the ground on the southern flank of the Alps. However, for weaker winds there are no clouds on the upwind side as a strong cold pool is responsible for the generation of convective cells far upstream of the ridge, in the Po valley, and for their propagation southward, similar to our experiment with $U = 2.5$ m s^{-1}.

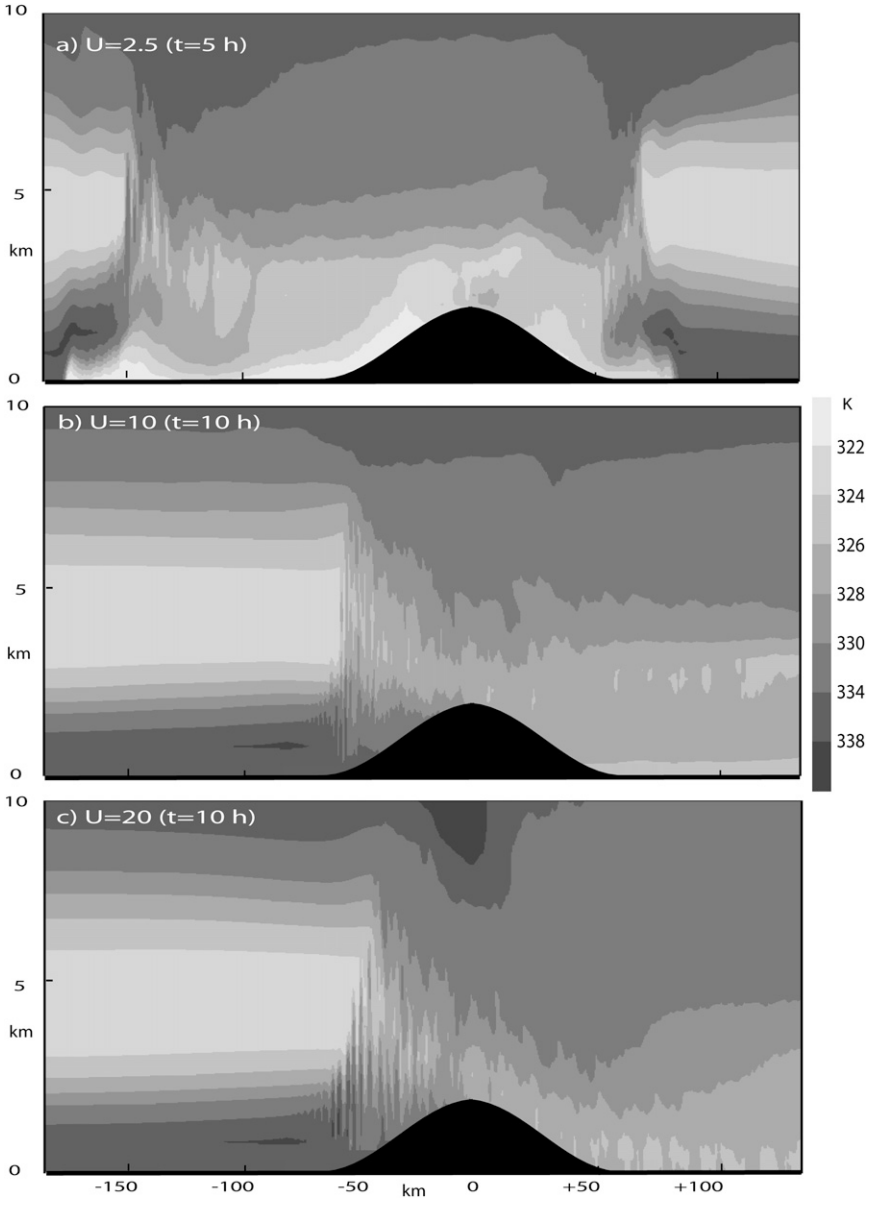

FIG. 7. Vertical cross sections (extending from the ground up to 10 km) of the y average of the equivalent potential temperature. The results are shown after $t = 5$ h in (a) and at the final integration time $t = 10$ h in (b) and (c).

b. *Parameter study: $U = 20$ m s^{-1} and the role of the Froude number*

In the previous subsection, we analyzed the dependence of the solution on the environmental wind speed U. In terms of the nondimensional numbers indicated in (2), a change in U means a change in DCAPE/U^2, CAPE/U^2, and h_mN/U. Thus, any of these parameters might be responsible for the differences observed in the flow features, and we cannot infer from the previous experiments which one of these nondimensional numbers has the most significant influence. However, we can easily check which of these parameters are not determining factors for the solution.

Figure 9 shows the solution features along a vertical cross section, as in Fig. 5, for two experiments with different U and h_m but with h_mN/U kept constant; Fig. 9a shows the results for $U = 2.5$ m s^{-1} and $h_m = 500$ m whereas Fig. 9b shows those for $U = 10$ m s^{-1} and $h_m = 2000$ m (as in Fig. 5b). The temperature profiles and the mountain half-widths ($a = 30$ km) are kept the same in the two simulations. It is apparent that the solution

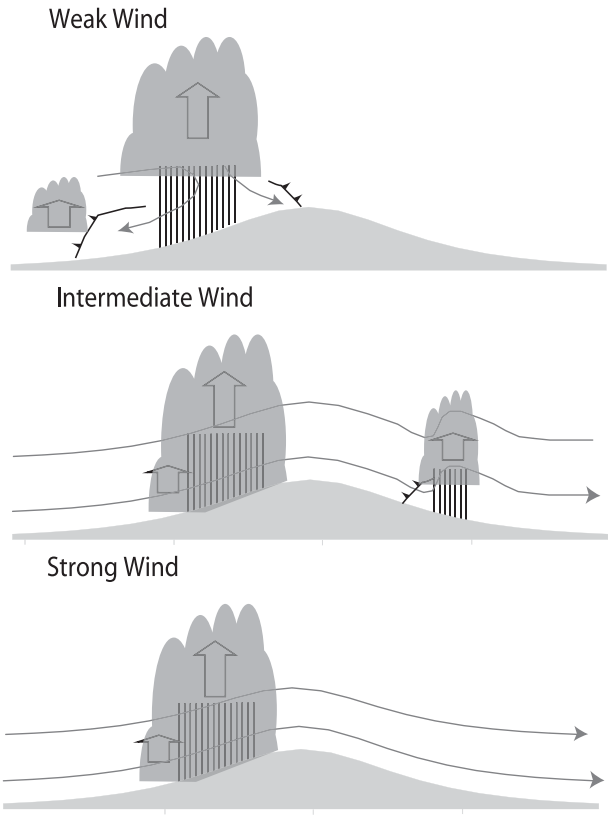

FIG. 8. Explanation of the effect of the wind speed on the solution. For weak wind, the rainfall generated on the upstream side of the ridge may evaporate into midlevel, potentially cool air, which can descend to the surface and subsequently produce a cold outflow. For larger wind speeds, the net cooling from evaporation is small compared to the advection of ambient potential temperature to the windward face of the ridge, so that the decrease in potential temperature is minimal. For the intermediate wind case, convection is triggered downstream; rain evaporates into the descending low-θ_e air and produces a stationary cold pool.

regime is completely different: density currents propagate upstream and downstream in Fig. 9a, similar to the experiment shown in Fig. 5a (for the same value of $U = 2.5$ m s^{-1}), whereas a quasi-stationary downstream current is present in Fig. 9b. Similar results occur for other values of h_mN/U, showing that there is no significant dependency of the solution on the Froude number (U/h_mN) in this particular convective regime. We will return to the theme of the nondimensional parameter dependence of the solutions in section 4.

In the remainder of this section, we discuss different experiments performed by changing the value of U, h_m, and a. To have a uniform standard of comparison, the y-averaged rain rate (calculated in the time interval from 5 to 10 h) is shown for all cases. Figure 10a refers to experiments with $U = 20$ m s^{-1}, $h_m = 2000$ m, and different a. For a narrower ridge ($a = 15$ km), the convective rainfall is mainly concentrated slightly upstream and over the ridge top; for $a = 30$ km, the rainfall is distributed over a wider area with a secondary maximum far upstream and the main peak just downwind of the ridge top; for $a = 60$ km, the area covered by rainfall is even larger with the rainfall maximum positioned slightly upstream of the ridge top.

An explanation for these solution features is provided in Fig. 11. Convective cells develop at the location (X_{cell}) where the orographic forcing lifts the low-level parcels above the LFC. Because the distance of X_{cell} from the ridge top increases with a, for narrower ridges the first cells form immediately upstream (at $x \sim -a$) of the ridge top; and because the advective time scale a/U ($\sim$1500 s) is comparable with the cell time scale $\sim h_t/(\text{CAPE})^{1/2}$ ($\sim$300 s), the rainfall maximum occurs very close to the ridge top. For wider mountains [thus, $a/U \gg h_t/(\text{CAPE})^{1/2}$], a first group of cells develops far upstream and is responsible for the secondary maximum close to X_{cell}; however, there is enough distance between X_{cell} and the ridge top for the development of another group of convective cells closer to the ridge; this distance determines whether the location of the secondary group is on the upwind slope (as for $a = 60$ km) or rather slightly on the downwind side (as for $a = 30$ km) of the ridge. These results indicate that the location of heavy rainfall is sensitive to the location where the first convective cells develop (see also Yoshizaki and Ogura 1988).

Figure 10b shows the solution features for $h_m = 1000$ m. With respect to the case with $h_m = 2000$ m, the rainfall pattern is shifted downstream: for $a = 15$ km, no rainfall is observed upstream; for $a = 30$ km, the precipitation is confined close to the ridge top and, in contrast with Fig. 10a, only one rainfall maximum occurs, located slightly upstream; for $a = 60$ km, two rainfall peaks of comparable intensity are present, but both are shifted downstream with respect to similar features in Fig. 10a.

Figure 12 explains the behavior as a function of the ridge height emerging from the comparison of Fig. 10a with Fig. 10b. For shorter ridges, h_m/LFC is smaller, thus the uplift required to trigger convection is reached closer to the ridge top and the rainfall pattern is shifted downstream: considering the time required for the cells to develop, one can understand the absence of upstream rainfall for the case $a = 15$ km (Fig. 10b). For $a = 30$ km, the reduction of the number of precipitation maxima from two to one passing from $h_m = 2000$ m to $h_m = 1000$ m can be similarly understood: for the shorter ridge, the first cells develop closer to the ridge top; considering that the resulting downdrafts occur farther downstream, on the downwind side of the ridge top, a further group of

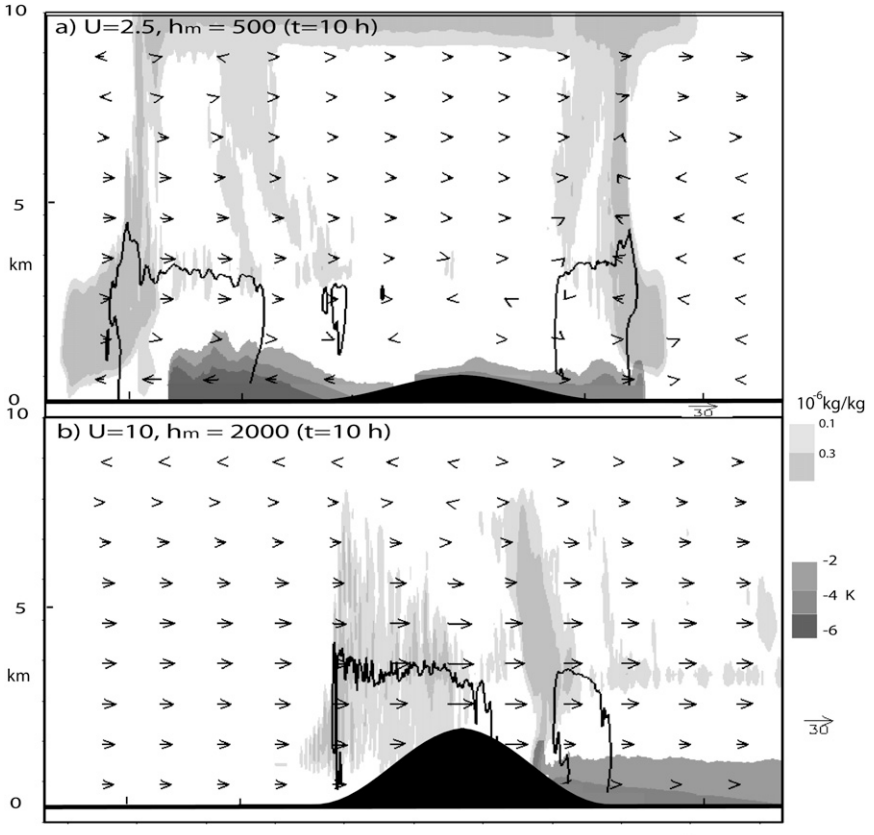

FIG. 9. As in Fig. 5 but for experiments with $a = 30$ km and (a) $U = 2.5$ m s^{-1} and $h_m = 500$ m and (b) $U = 10$ m s^{-1} and $h_m = 2000$ m. The two experiments correspond to the same value of h_mN/U.

cells that might have been triggered is instead suppressed by the downward motion associated with the orographic forcing.

This tendency toward a downstream shifting of the rainfall pattern, observed in passing from $h_m = 2000$ m to $h_m = 1000$ m, is still present moving to yet a smaller ridge height, as shown in Fig. 10c for $h_m = 500$ m. For the particular case $a = 15$ km, the absence of convection in the stationary solution is apparent. The explanation for this case is provided in Fig. 13: When h_m is less than the LFC, the triggering of convective cells will occur, if it does, close to the ridge top; in the case of the narrower ridge, it may even occur on the downwind side of the ridge top where the ascending convective motion competes with the descending motion induced by the ridge, and hence the convection may eventually be suppressed (hence the question mark in the downstream cloud).

The experiments shown so far describe the flow response for different h_m and a with wind speed fixed. Now we continue with the examination of the solution space for other values of U.

c. *Parameter study: $U = 10$ m s^{-1}*

Figure 14 shows the y-averaged rain rate for different a and h_m, as in Fig. 10, but for $U = 10$ m s^{-1}. Compared with case for $U = 20$ m s^{-1} shown in Fig. 10a, Fig. 14a for $a = 15$ km shows that a secondary rainfall maximum now occurs downstream, associated with a slowly downstream-propagating cold pool. Figure 14a shows that for $a = 15$ km this maximum remains quasi-stationary on the downwind slope (near $x \sim +20$ km), almost merging with the main precipitation peak, whereas for the wider ridge, $a = 30$ km, the downstream rainfall maximum is weaker and located farther downstream (near $x \sim +50$ km). For the widest ridge, $a = 60$ km, this feature becomes very weak. Comparing the upstream features for different values of a, the solutions suggest that the wider is the ridge, the farther upstream is the precipitation; thus, the explanation provided in Fig. 11 is also valid in the present case with $U = 10$ m s^{-1}.

We note that for $a = 60$ km the rainfall pattern is less stationary as compared to the corresponding case with

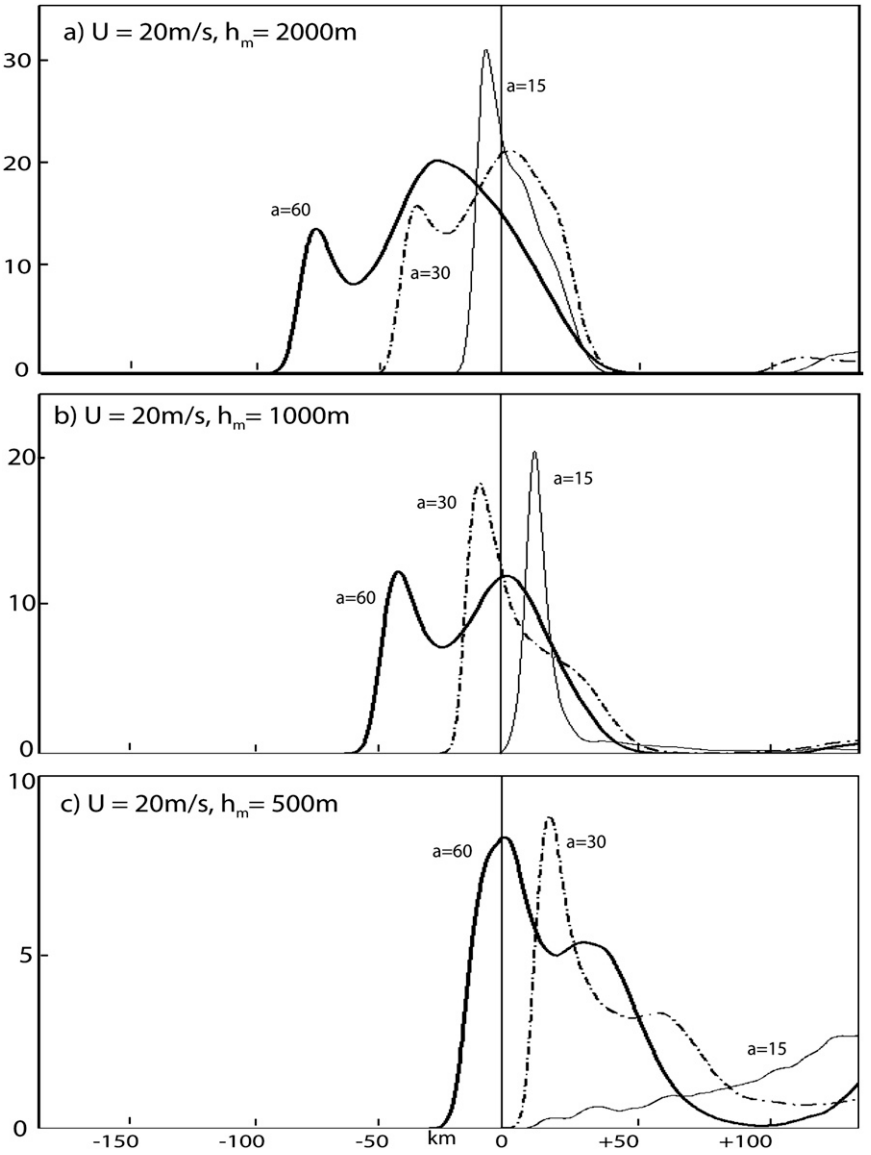

FIG. 10. Rain rate calculated in the time interval between 5 and 10 h for experiments with $U = 20$ m s^{-1} and $h_m =$ (a) 2000 m, (b) 1000 m, and (c) 500 m.

$U = 20$ m s^{-1}, especially far upstream where the location of the rainfall changes in a regular way in the latter case. This greater irregularity can be explained as a consequence of the smaller orographically induced condensation when the wind speed is weaker and a larger, which allows rain evaporation and thus the generation of a cold potential temperature perturbation upstream (not shown). However, the upstream environment is still close to saturation and the ambient wind speed is relatively strong so that the cold pool remains weak and cannot propagate far from the ridge.

Figure 14b shows the rain rate for $h_m = 1000$ m. In this case, the downstream cold pool propagates upstream against the main flow with its head reaching the upwind slope (not shown): for this ridge height this feature was not present in the CL2000 experiments (we verified that this feature is not due to a spurious reflection from the outflow boundary by doubling the domain length in our simulation). The upstream propagation is more apparent for the wider ridge since in that case the orographic downslope wind is weaker and cannot counterbalance the movement of the cold pool. With respect to Fig. 14a, the location of the precipitation in Fig. 14b shifts farther downwind for smaller values of h_m, consistent with the mechanism illustrated in Fig. 13 for $U = 20$ m s^{-1}.

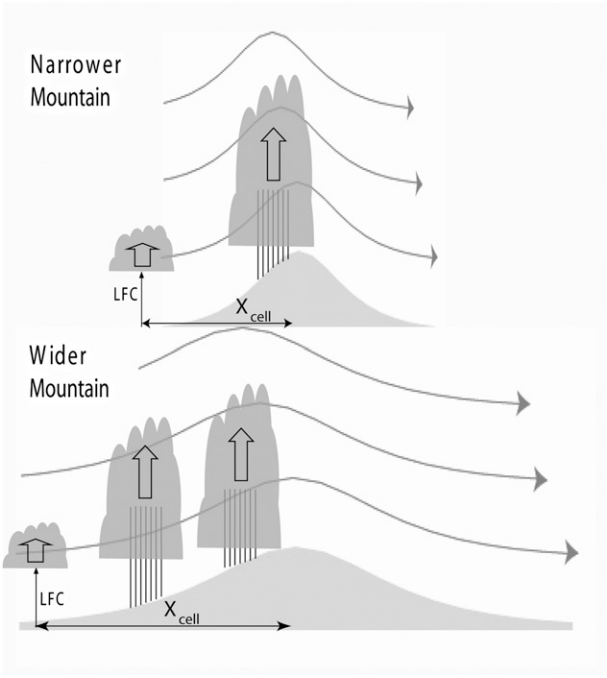

FIG. 11. Explanation of the effect of the ridge half-width a on the solution. A wider ridge has the effect of spreading the precipitation over a larger region, as the LFC is reached by the low level parcels far upstream of the ridge.

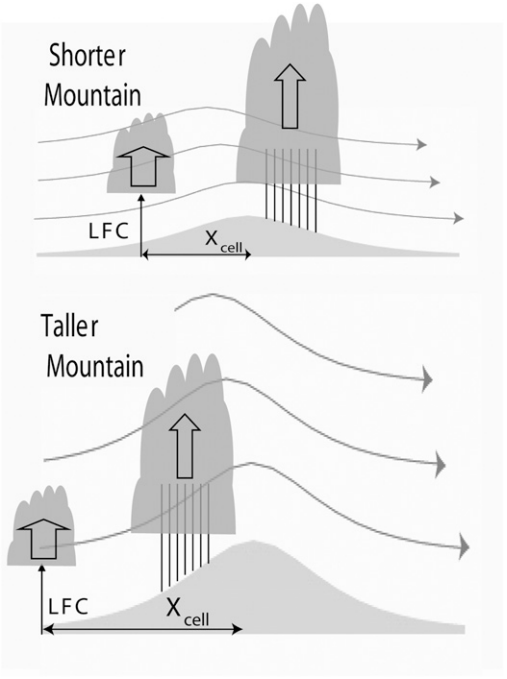

FIG. 12. Explanation of the effect of the maximum ridge height h_m on the solution. For short ridges, the uplift required to trigger convection is reached closer to the ridge top and the rainfall pattern is shifted downstream.

Finally, Fig. 14c shows the results for $U = 10$ m s^{-1} and $h_m = 500$ m. In this case, the upstream propagation of the density current moving from the downwind side, as shown in Fig. 14b, is a feature of the solution for all the values of a. Thus, the downstream shift of the precipitation for shorter ridges is balanced by the upstream propagation of the cold pool and the location of the precipitation after 10 h is close to that observed in Fig. 14b. In contrast with the case $U = 20$ m s^{-1} and $a =$ 15 km (Fig. 10c) in which no precipitation occurs close to the ridge, Fig. 14c shows that, for the weaker wind speed (with a larger advective time scale a/U), the time the parcels spend after passing the LFC and before reaching the ridge top is long enough to allow the growth of deep convective cells.

In conclusion, the type of flow illustrated in Fig. 5b is representative of the basic flow features observed in all the experiments for $U = 10$ m s^{-1}, which are the presence of upstream quasi-stationary convective cells and a downstream cold pool. The behavior of the cold pool changes according to the ridge dimensions: in particular, for shorter and wider ridges, associated with a weaker orographic downslope wind, the density current can propagate against the ambient flow and reach the upwind side of the ridge, whereas for high ridges the cold pool remains confined downstream.

Compared with the cases with $U = 20$ m s^{-1} (Fig. 10) the rain rate for the cases with $U = 10$ m s^{-1} (Fig. 14) shows two distinct upstream rainfall maxima due to the larger advective time scale, which allows the development of two distinct groups of convective cells upstream of the ridge. Another difference is the smaller change in the precipitation maximum occurring among the experiments with $U = 10$ m s^{-1} due to the upstream movement of the downstream density current in many cases with $h_m \leq 1000$ m.

The same sensitivity analysis was also performed in the case $U = 2.5$ m s^{-1}. For this wind speed, the solution features are almost independent of h_m, at least for $h_m \gtrsim$

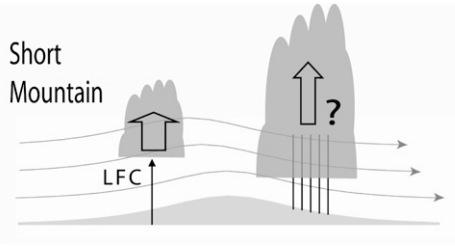

FIG. 13. Explanation of the absence of quasi-stationary rain in case of short and narrow ridges. The triggering may occur downslope, where the descending motion induced by the ridge may suppress the development of the cells.

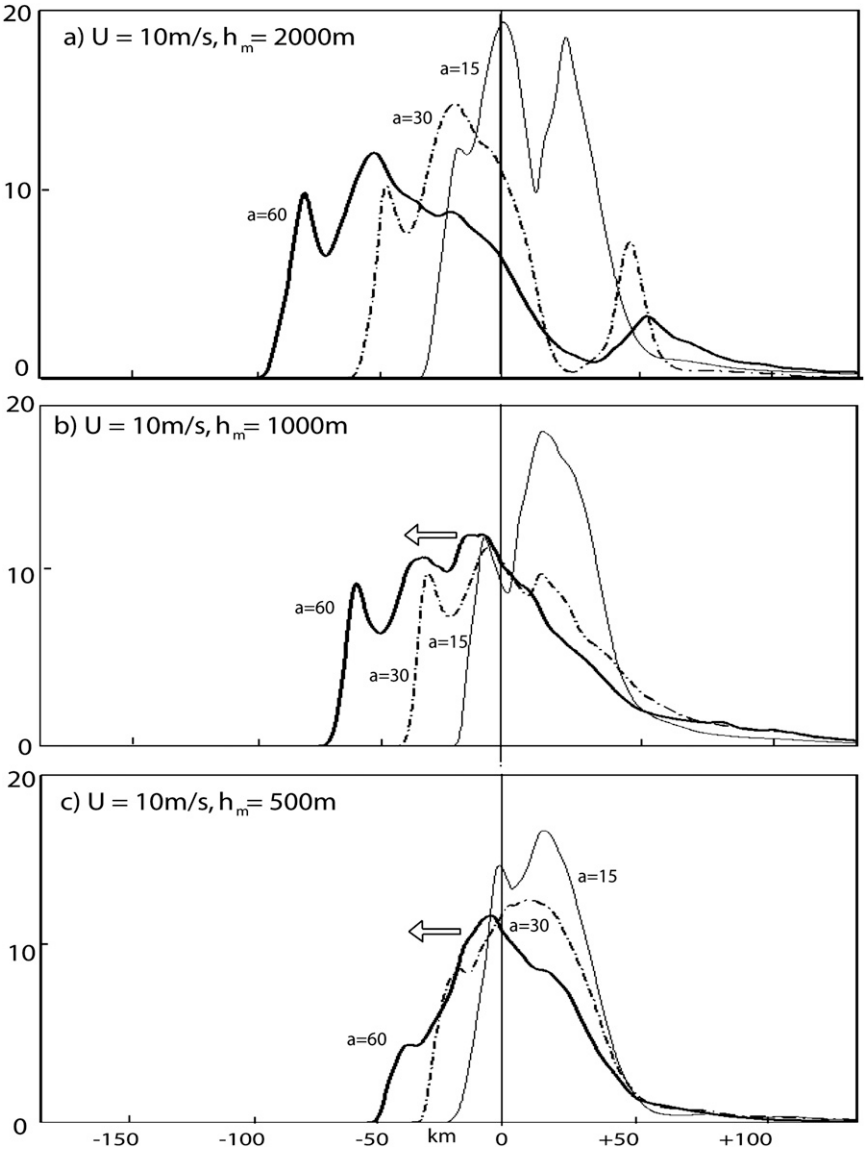

FIG. 14. As in Fig. 10 but for $U = 10$ m s^{-1}.

LFC, and are similar to those shown in Figs. 5a and 6a. For ridges shorter than the LFC, the uplift induced by the small wind speed is not sufficient to generate any convective cells close to the ridge even for narrow ridges, as illustrated in Fig. 13. Similar results occur in simulations with $U = 5$ m s^{-1} (not shown).

4. Precipitation

As one of the basic motivations of this work is the analysis of precipitation, it is of interest to see how the differing flow responses affect the rainfall rate. Estimation of precipitation based on orographically induced uplift (Smith 1979; Rotunno and Ferretti 2001) does not work in the present case owing to the different mechanisms associated with cumulus convection in contrast with orographic uplift in stable or neutral environments.

To compare the rainfall rates among the different experiments we will analyze the y average of the maximum precipitation R_m and of the total rainfall R_{tot}: the latter parameter is the integral of the y-averaged rain rate (calculated in the time interval from 5 to 10 h) along the area of the channel from $x = -80$ km to $x = +40$ km around the ridge peak. The value shown in Table 1 is obtained after division by the integral length (120 km) and thus its value is expressed in millimeters. To provide a more complete exploration of the parameter space and thus more definite conclusions, further simulations have been performed. The complete list of all the experiments

is shown in Table 1. In our analysis we will count the rainfall amount only in those experiments presenting a (quasi-) stationary precipitation pattern; otherwise it is set to zero.

From the point of view of dimensional analysis, the maximum rainfall rate R_m (and similarly the total rainfall $R_{\rm tot}$) can be related to the input parameters through a functional relation depending on the nondimensional numbers identified in (2) (or, of course, on any other grouping of them), of the type

$$R_m/\rho_{v,s}U = G_M(\cdots), \tag{3}$$

where $\rho_{v,s}$ is the upstream surface vapor density.

As mentioned in section 2a, it was not possible in this study to explore the full dependence of the rain rate on all the arguments shown in (3); thus, we will try to narrow the range of possible sensitivities and characterize the function g_m, that is, the projection of G_M onto a subspace consisting of only those parameters to which we believe the rainfall amount and distribution are most sensitive. Based on experience we believe such a subset of parameters should include at least h_m, a, U, and CAPE in some combination, as we showed in section 3 that variation of these parameters significantly influences solutions.

The first parameter we consider is related to the triggering of convective cells and is proportional to h_m/LFC. In fact, when h_m/LFC $\ll 1$, the cells cannot develop, as shown in Figs. 10c and 13. The sensitivity of the solutions to h_m, as illustrated in Fig. 12, suggests that the intensity and distribution of the rainfall strongly depend on this nondimensional number.

Another argument of the function g_m should be related to the orographic forcing ($\sim Uh_m/a$). For $U = 10$ m s^{-1}, Table 1 shows that R_m generally decreases with increasing a, whereas the dependence of R_m on h_m, and also of $R_{\rm tot}$ on a and h_m, is not straightforward. For the case $U = 20$ m s^{-1}, Table 1 also indicates that R_m generally increases with h_m and decreases with increasing a, while $R_{\rm tot}$ is directly proportional both to h_m and a. Thus, if we consider only the simulations with $U = 20$ m s^{-1} (and constant CAPE), the dependence of R_m on Uh_m/a is approximately linear. In the stable case, the reason for this proportionality would be easily understood since the ascending motion produced by the orography is directly responsible for the condensation rate above the terrain (Smith 1979; Rotunno and Ferretti 2001). However, in the convective case the orographic forcing has no direct effect on the intensity of the updrafts that are $\sim$(CAPE)$^{1/2}$, which are mainly responsible for the rainfall under unstable conditions; in other words, since $Uh_m/a \ll$ (CAPE)$^{1/2}$, the contribution of the direct orographic forcing to uplift, and hence to condensation rates, can be considered to be minor (cf. Chen and Lin 2005). Our analysis shows that the linear dependence of R_m on Uh_m/a for the greater wind speed is due to the more uniform distribution of cells in the along-ridge direction, which naturally gives a larger value of the along-ridge mean value of R_m. In fact, with weaker winds the production of cold pools and the longer advective time scale allow for more spatial and temporal variability in the orographic convection. Hence, we will include the nondimensional parameter h_m/a in our analysis but with the expectation of a nontrivial dependence g_m (h_m/a).

Finally, the data suggests including a parameter that depends on U and CAPE. Table 1 shows that the rainfall peak generally increases with wind speed, while the relation with CAPE is more complex; in fact, for $U =$ 20 m s^{-1} the maximum and the total rainfall are almost independent of CAPE, whereas for $U = 10$ m s^{-1} both the fields increase with CAPE. The stronger uplift occurring for larger CAPE can easily explain the results for $U = 10$ m s^{-1}, while in the case $U = 20$ m s^{-1} the stronger forcing is partially counterbalanced by the unfavorable location of the cells in the leeside downslope flow (not shown).

The simplest way to express the dependence of R_m on these parameters is to include U/(CAPE)$^{1/2}$ as a nondimensional argument. However, two dimensional parameters can be combined to produce a more physically meaningful number, which is the ratio of the advective time scale $\tau_a = a/U$ to a time scale representative of the convective cell, $\tau_c \sim h_t$/(CAPE)$^{1/2}$. In fact, we have already used the ratio of these two time scales to explain the occurrence and the location of the cells. When $\tau_a/\tau_c < 1$, there is not enough time for the development of any cell upstream of the obstacle; when $\tau_a/\tau_c \sim O(1)$, some groups of cells may develop upstream; for $\tau_a/\tau_c \gg 1$ (e.g., for very small U), several cells can be generated far upstream of the ridge; in this case, the environment is favorable to the development of cold pools and the solution has no rain occurring near the ridge. In conclusion, the function we will try to characterize is of the form

$$R_m/\rho_{v,s}U = g_M[h_m/\text{LFC},\ h_m/a,\ a/U(\text{CAPE})^{1/2}/h_t]. \tag{4}$$

Figures 15 and 16 show respectively the dependence of $R_m/\rho_{v,s}U$ and its position X_m/a on h_m/LFC and h_m/a in two-dimensional plots for different values of $\tau_a/\tau_c = a/U(\text{CAPE})^{1/2}/h_t$. Consistent with the illustration given in Fig. 13, Fig. 15 indicates that for h_m/LFC < 0.3, $R_m/\rho_{v,s}U = 0$ for all τ_a/τ_c . This result has been checked in some additional numerical experiments performed for low values of h_m/LFC and not included in Table 1. For h_m/LFC > 0.3, Fig. 15 indicates a radically different

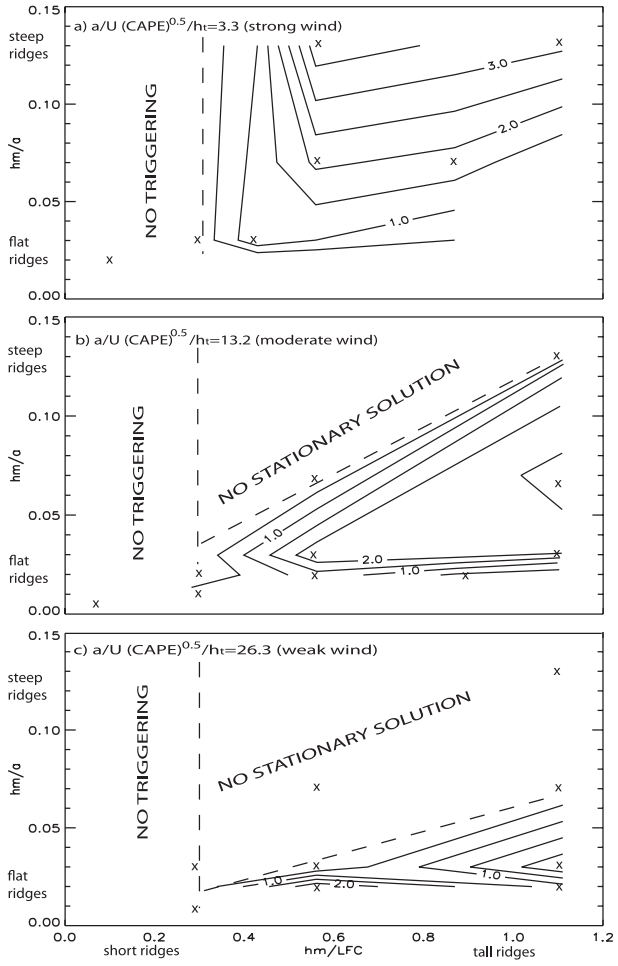

FIG. 15. Plot of $R_m/\rho_{v,s}U \times 10^2$ (contour interval = 0.5) vs h_m/LFC and h_m/a for $\tau_a/\tau_c = a/U(\text{CAPE})^{1/2}/h_t$ = (a) 3.3, (b) 13.2, and (c) 26.3.

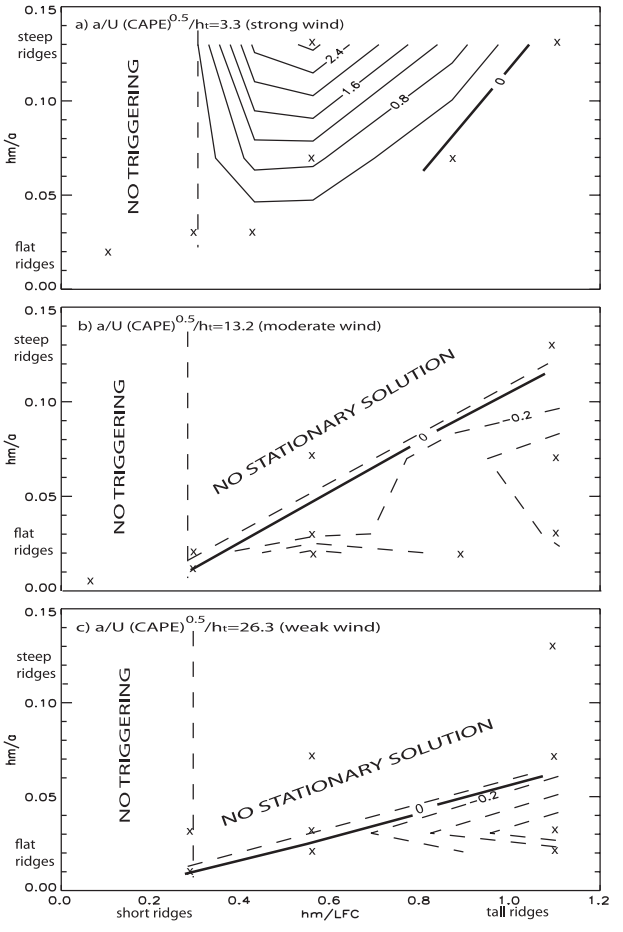

FIG. 16. As in Fig. 15 but for X_m/a. Dashed lines correspond to negative values and denote upstream locations of the precipitation peak; continuous lines correspond to positive values and denote downstream locations; bold lines correspond to zero and refer to location of the rainfall over the top of the ridge.

dependence of $R_m/\rho_{v,s}U$ on h_m/LFC and h_m/a for the differing τ_a/τ_c.

Considering first the smallest values of τ_a/τ_c (Figs. 15a, 16a), one observes generally increasing $R_m/\rho_{v,s}U$ with increasing h_m/a and increasing h_m/LFC, up to h_m/LFC ~0.6, after which $R_m/\rho_{v,s}U$ remains approximately constant. This regime of small τ_a/τ_c contains cases with stronger winds, narrower ridges, and weaker instability; hence, the locations of the peak rain rates tend to be on the downstream side of the ridge (Fig. 16a). The increase of along-ridge-averaged rain rate with slope is due to the more effective alignment of cells (as explained above) in these cases.

Considering next the intermediate value of τ_a/τ_c (Figs. 15b, 16b), one observes that $R_m/\rho_{v,s}U$ no longer increases monotonically with h_m/a. This latter feature is due to the dominance of cold pools for taller, steeper mountains in the regime of weaker winds, broader ridges, and stronger instability. Hence, stationary rain over the ridge results from an optimum steepness h_m/a for a given h_m/LFC; Fig. 15b shows that this region of parameter space is confined close to the line defined by $h_m/a \sim 0.06\, h_m$/LFC, with larger values of precipitation as we move along the line away from the origin. Consistent with our interpretation, Fig. 16b shows that the rainfall occurs on the upwind side of the ridge.

Finally, for the largest values of τ_a/τ_c (Figs. 15c, 16c), which correspond to the weakest winds, broadest ridges, and strongest instability, cold pools dominate, and therefore the solutions having steady rain over the ridge are restricted to an even smaller corner of the parameter space (Fig. 15c); these solutions are also characterized by peak rainfall on the upwind side of the ridge (Fig. 16c).

Figure 17 shows the dependence of the total rainfall $R_{\text{tot}}/\rho_{v,s}U$ on h_m/LFC and h_m/a for different τ_a/τ_c. Compared to $R_m/\rho_{v,s}U$, the functional relation in this

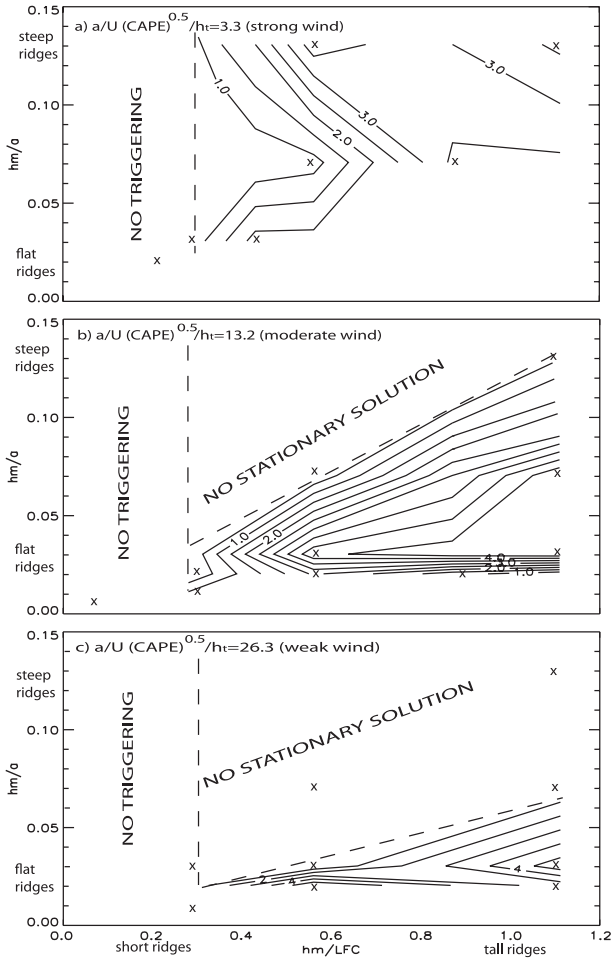

FIG. 17. As in Fig. 15 but for $R_{\text{tot}}/\rho_{v,s}U \times 10^2$. Contour interval is 0.5 in (a) and (b) and 1 in (c).

case is more complex. In fact, whereas for intermediate and large τ_a/τ_c the dependence is quite similar to that shown in Fig. 15, two distinct rainfall maxima occur for small values of τ_a/τ_c in the upper and in the lower right side of the plot. In particular, the latter maximum is due to high and wide ridges, which are able to spread the precipitation over a wide area, thus producing a large integral value although the peak is relatively small (see Fig. 15a).

5. Conclusions

Conditionally unstable flow over mountainous areas is a well-known element of heavy precipitation events, which sometimes lead to flash flooding (e.g., Lin et al. 2001). One of the central questions with respect to forecasting the latter is the determination of the conditions under which deep cumulus convection will precipitate over the same location. The difficulty in providing a definite answer to this question is due in part to the three-dimensional stochastic nature of turbulent convection in general, in part to the microphysics related with the production of precipitation, and in part to the often complex terrain features over which the convective clouds may form. The present study is an attempt to carry out a systematic study of three-dimensional precipitating cumulus convection as it may occur on a simple two-dimensional ridge. Using a three-dimensional numerical model, a number of external input parameters characterizing the simple topography and the ambient atmosphere were varied, and the response of the resulting along-ridge-averaged precipitation recorded. These results are summarized here.

The response of the system to different wind speeds U is characterized by two basically different types of solution. For small values of U ($= 2.5$ m s^{-1}), there is ample time for the initial convective cells to produce a cold pool through the evaporation of precipitation into the subsaturated midlevel air. A density current is then generated that spreads and forces the environmental air up and over its head (e.g., Fig. 5a). As the cold pool propagates away from the ridge, it induces new convective cells upstream, so no stationary precipitation occurs over the ridge. For larger values of U ($= 10$, 20 m s^{-1}), quasi-stationary convective cells are simulated on the upstream side of the ridge with no cold pool present (e.g., Figs. 5b,c). This response as a function of wind speed can be explained by considering that the net evaporative cooling on the windward slope depends on the environmental wind speed. For large U, there is little time for traveling parcels to cool substantially before reaching the ridge top and subsequent descent on the lee side.

For intermediate wind speeds ($U = 10$ m s^{-1}), a second set of convective cells is generated downwind by the convergence between the cold pool and the leeside flow (e.g., Fig. 5b). The balance between propagation speed of the density current and the value of the downslope wind determines the upwind movement of the cold pool. Thus, for shorter and wider ridges, associated with a weaker downslope wind, the density current can propagate against the flow and reach the upwind side of the ridge, whereas for higher ridges the downslope wind is strong enough to counterbalance the cold-pool propagation, so it remains quasi-stationary on the downstream side of the ridge.

The effect of the topography on the solution was also systematically explored. A significant sensitivity for any value of U, a, or CAPE was that, for $h_m \ll$ LFC, the orographic uplift was not sufficient to trigger any convective cell. With $h_m >$ LFC, the solution exhibited a significant sensitivity to a: for $U = 10$ m s^{-1} and $U = 20$

m s^{-1} (no cold pool far upstream), the wider the ridge, the larger the region affected by precipitation, as the LFC is reached by parcels farther upstream of the ridge top. Moreover, a narrow, short ridge produced a precipitation pattern shifted downstream with respect to a wider, higher ridge, as the LFC is reached closer to the ridge top with subsequent cell growth and precipitation occurring farther downstream. Hence, the ratio between the advective time scale, $\tau_a = a/U$, and the convective time scale, $\tau_c = h_t/(\text{CAPE})^{1/2}$, and h_m/LFC emerged as two important control parameters. Finally, the solutions showed significant sensitivity to the slope h_m/a since the stronger the orographic uplift, the greater the tendency for cells to be aligned along the ridge and, hence, the greater the along-ridge-averaged precipitation.

The above-described sensitivity of the along-ridge-averaged precipitation to variations in U, h_m, a, or CAPE was summarized using dimensional analysis through its dependence on the parameters h_m/LFC, h_m/a, and τ_a/τ_c as shown in Figs. 15–17. This result is consistent with the finding that ''the location of heavy precipitation relative to the ridge peak is expected to vary depending on several factors. These factors include the lifting required for an air parcel to reach the LFC, the distance that a convective cell travels toward the ridge peak before it attains a mature stage of development, and the terrain shape'' (Yoshizaki and Ogura 1988). Experiments performed with different ridges and environmental wind speeds, but with the same value of the Froude number U/h_mN, show completely different flow responses.

Comparing our simulations with the experiments performed in CL2000 and Chen and Lin (2005), some differences emerge both as a consequence of the present finer horizontal resolution and three-dimensionality of our simulations. Our exploratory experiments performed with a coarser horizontal resolution or 2D geometry show that some specific details of the solutions (in particular, precipitation distribution and amount) may change significantly. However, the different flow regimes addressed in those papers are at least qualitatively reproduced in our simulations. The most important differences concern the explanation of those regimes. In the above-cited papers, the cold pool produced by precipitating cell is taken as a more-or-less constant element that is swept farther downstream as the ambient winds increase. Our analysis (section 3a) shows, however, that with increasing wind there is not enough time for traveling cells to produce significant net evaporation and, therefore, cold pools.

Comparing our results with observed-case-oriented experiments, initialized with semi-idealized atmospheric profiles (Stein 2004; Davolio et al. 2006), we find the following points of similarity. For example, in numerical experiments using a single idealized conditionally unstable sounding and constant wind over the actual alpine topography, Stein (2004) found that for a large wind speed, clouds develop upwind of the ridge and the flow passes over the Alps; for weak wind speeds, a cold pool is responsible for the propagation of the rain southward (upwind) of the Alps.

Finally, we note again the limitations of the present study. We verified that some experiments performed with different CAPE and U but almost the same value of the three selected nondimensional parameters show different rainfall amounts, suggesting that the function g_M probably should include, in some way, other sounding parameters in the set of its arguments; we are currently doing additional experiments to explore the possible further dependencies. These differences seem to be partially explained by the tendency toward static-stability-dominated orographic flow in the limit of low-CAPE environments; this regime will be better addressed in a forthcoming paper. Finally, attention has been devoted to a single class of upstream profiles with uniform upstream wind speed. To represent a more realistic atmosphere, one should include inversions and vertical wind shear, which may significantly affect the formation and the development of convective cells. The analysis of the role of the wind shear and a deeper investigation of the sounding parameters will be the subject of a future work.

Acknowledgments. The stay of M. Miglietta in Boulder was supported in part by NCAR and in part by the EU project ''Weather Risk Reduction in the Central and Eastern Mediterranean'' (RISKMED). Comments by George Bryan and Morris Weisman on the first draft of this paper are gratefully acknowledged.

REFERENCES

Braun, S. A., and W.-K. Tao, 2000: Sensitivity of high-resolution simulations of Hurricane Bob (1991) to planetary boundary layer parameterizations. *Mon. Wea. Rev.,* **128,** 3941–3961.

Bryan, G. H., and J. M. Fritsch, 2002: A benchmark simulation for moist nonhydrostatic models. *Mon. Wea. Rev.,* **130,** 2917–2928.

——, J. C. Wyngaard, and J. M. Fritsch, 2003: Resolution requirements for the simulation of deep moist convection. *Mon. Wea. Rev.,* **131,** 2394–2415.

——, J. C. Knievel, and M. D. Parker, 2006: A multimodel assessment of RKW theory's relevance to squall-line characteristics. *Mon. Wea. Rev.,* **134,** 2772–2792.

——, R. Rotunno, and J. M. Fritsch, 2007: Roll circulations in the convective region of a simulated squall line. *J. Atmos. Sci.,* **64,** 1249–1266.

Byers, H. R., and R. R. Braham Jr., 1949: *The Thunderstorm*. U.S. Government Printing Office, 287 pp.

Caracena, F., R. A. Maddox, L. R. Hoxit, and C. F. Chappell, 1979: Mesoanalysis of the Big Thompson storm. *Mon. Wea. Rev.,* **107,** 1–17.

Chen, S.-H., and Y.-L. Lin, 2005: Effects of moist Froude number and CAPE on a conditionally unstable flow over a mesoscale mountain ridge. *J. Atmos. Sci.,* **62,** 331–350.

Chu, C. M., and Y.-L. Lin, 2000: Effects of orography on the generation and propagation of mesoscale convective systems in a two-dimensional conditionally unstable flow. *J. Atmos. Sci.,* **57,** 3817–3837.

Davolio, S., A. Buzzi, and P. Malguzzi, 2006: Orographic influence on deep convection: Case study and sensitivity experiments. *Meteor. Z.,* **15,** 215–223.

Deardorff, J. W., 1980: Stratocumulus-capped mixed layer derived from a three-dimensional model. *Bound.-Layer Meteor.,* **18,** 495–527.

Droegemeier, K. K., Y. P. Richardson, G. M. Bassett, and A. Marroquin, 1997: Three-dimensional numerical simulations of turbulence generated in the near-environment of deep convective storms. Preprints, *Seventh Conf. on Aviation, Range, and Aerospace Meteorology*, Long Beach, CA, Amer. Meteor. Soc, 169–174.

Durran, D. R., 1986: Another look at downslope windstorms. Part I: The development of analogs to supercritical flows in an infinitely deep, continuously stratified flows. *J. Atmos. Sci.,* **43,** 2527–2543.

——, and J. B. Klemp, 1983: A compressible model for the simulation of moist mountain waves. *Mon. Wea. Rev.,* **111,** 2341–2361.

Gilmore, M. S., and L. J. Wicker, 1998: The influence of midtropospheric dryness on supercell morphology and evolution. *Mon. Wea. Rev.,* **126,** 943–958.

Kirshbaum, D. J., G. H. Bryan, R. Rotunno, and D. R. Durran, 2007a: The triggering of orographic rainbands by small-scale topography. *J. Atmos. Sci.,* **64,** 1530–1549.

——, R. Rotunno, and G. H. Bryan, 2007b: The spacing of orographic rainbands triggered by small-scale topography. *J. Atmos. Sci.,* **64,** 4222–4245.

Klemp, J. B., and R. B. Wilhelmson, 1978: The simulation of three-dimensional convective storm dynamics. *J. Atmos. Sci.,* **35,** 1070–1096.

Lin, Y.-L., R. D. Farley, and H. D. Orville, 1983: Bulk parameterization of the snow field in a cloud model. *J. Climate Appl. Meteor.,* **22,** 1065–1092.

——, S. Chiao, T.-A. Wang, M. L. Kaplan, and R. P. Weglarz, 2001: Some common ingredients for heavy orographic rainfall. *Wea. Forecasting,* **16,** 633–660.

Miglietta, M. M., and R. Rotunno, 2007: Numerical simulations of conditionally unstable flows over a ridge. *Proc. 29th Int. Conf. on Alpine Meteorology*, Chambéry, France, Météo-France, 87–90.

Petch, J. C., A. R. Brown, and M. E. B. Gray, 2002: The impact of horizontal resolution on the simulations of convective development over land. *Quart. J. Roy. Meteor. Soc.,* **128,** 2031–2044.

Pontrelli, M. D., G. H. Bryan, and J. M. Fritsch, 1999: The Madison County, Virginia, flash flood of 27 June 1995. *Wea. Forecasting,* **14,** 384–404.

Reeves, H. D., and Y.-L. Lin, 2007: The effects of a mountain on the propagation of a preexisting convective system for blocked and unblocked flow regimes. *J. Atmos. Sci.,* **64,** 2401–2421.

Richard, E., A. Buzzi, and G. Zängl, 2007: Quantitative precipitation forecasting in the Alps: The advances achieved by the Mesoscale Alpine Programme. *Quart. J. Roy. Meteor. Soc.,* **133,** 831–846.

Romero, R., C. A. Doswell III, and C. Ramis, 2000: Mesoscale numerical study of two cases of long-lived quasi-stationary convective systems over eastern Spain. *Mon. Wea. Rev.,* **128,** 3731–3751.

Rotunno, R., and R. Ferretti, 2001: Mechanisms of intense Alpine rainfall. *J. Atmos. Sci.,* **58,** 1732–1749.

Schroeder, T. A., 1977: Meteorological analysis of an Oahu flood. *Mon. Wea. Rev.,* **105,** 458–468.

Sénési, S., P. Bougeault, J.-L. Chèze, P. Cosentino, and R.-M. Thepenier, 1996: The Vaison-La-Romaine flash flood: Mesoscale analysis and predictability issues. *Wea. Forecasting,* **11,** 417–442.

Smith, R. B., 1979: The influence of mountains on the atmosphere. *Advances in Geophysics,* Vol. 21, 87–230.

Stein, J., 2004: Exploration of some convective regimes over the Alpine orography. *Quart. J. Roy. Meteor. Soc.,* **130,** 481–502.

Walser, A., D. Lüthi, and C. Schär, 2004: Predictability of precipitation in a cloud-resolving model. *Mon. Wea. Rev.,* **132,** 560–577.

Weisman, M. L., and J. B. Klemp, 1982: The dependence of numerically simulated convective storms on vertical wind shear and buoyancy. *Mon. Wea. Rev.,* **110,** 504–520.

Wicker, L. J., and W. C. Skamarock, 2002: Time splitting methods for elastic models using forward time schemes. *Mon. Wea. Rev.,* **130,** 2088–2097.

Yoshizaki, M., and Y. Ogura, 1988: Two- and three-dimensional modelling studies of the Big Thompson storm. *J. Atmos. Sci.,* **45,** 3700–3722.

CORRIGENDUM

MARIO MARCELLO MIGLIETTA

Institute of Atmospheric Sciences and Climate (ISAC), Italian National Research Council (CNR), Lecce/Padua, Italy

RICHARD ROTUNNO

NCAR, Boulder, Colorado*

Incorrect versions of Figs. 5 and 9 were published in Miglietta and Rotunno (2009). The correct figures are shown below.

The authors regret any inconvenience this error may have caused.

REFERENCE

Miglietta, M. M., and R. Rotunno, 2009: Numerical simulations of conditionally unstable flows over a mountain ridge. *J. Atmos. Sci.,* **66,** 1865–1885.

* The National Center for Atmospheric Research is sponsored by the National Science Foundation.

Corresponding author address: Mario Marcello Miglietta, CNRISAC, Strada Provinciale Lecce-Monteroni, Km 1.200, 73100 Lecce, Italy.
E-mail: m.miglietta@isac.cnr.it

DOI: 10.1175/2009JAS3304.1

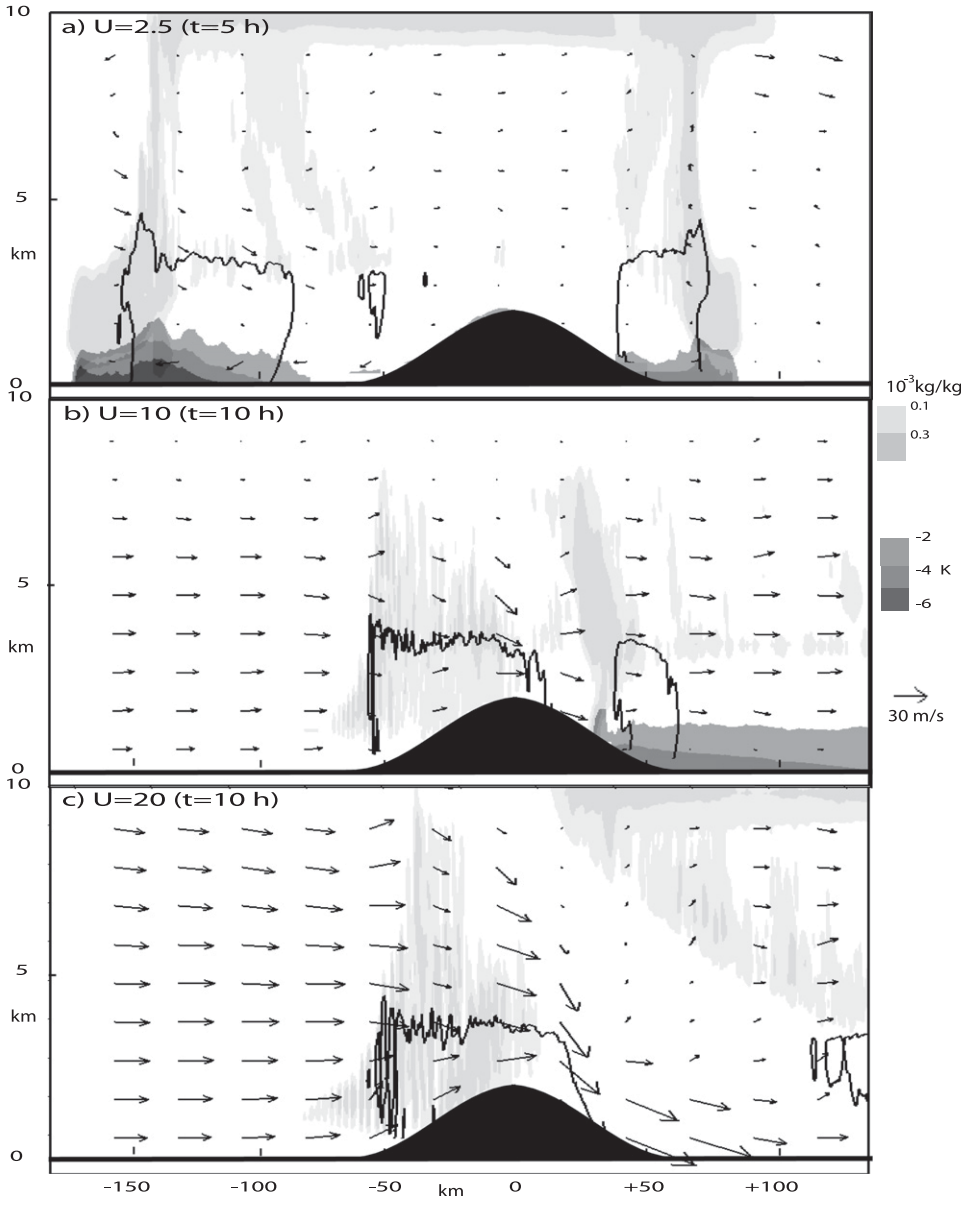

FIG. 5. Vertical cross sections (extending from the ground up to 10 km) of the y average of potential temperature perturbation (dark shaded areas), cloud water plus ice content (light shaded areas), rainwater content (contour line for 0.2×10^{-3} kg kg^{-1}), and wind speed (arrows) for the experiments shown in Fig. 3. The results are shown (a) after $t = 5$ h and (b),(c) at the final integration time $t = 10$ h.

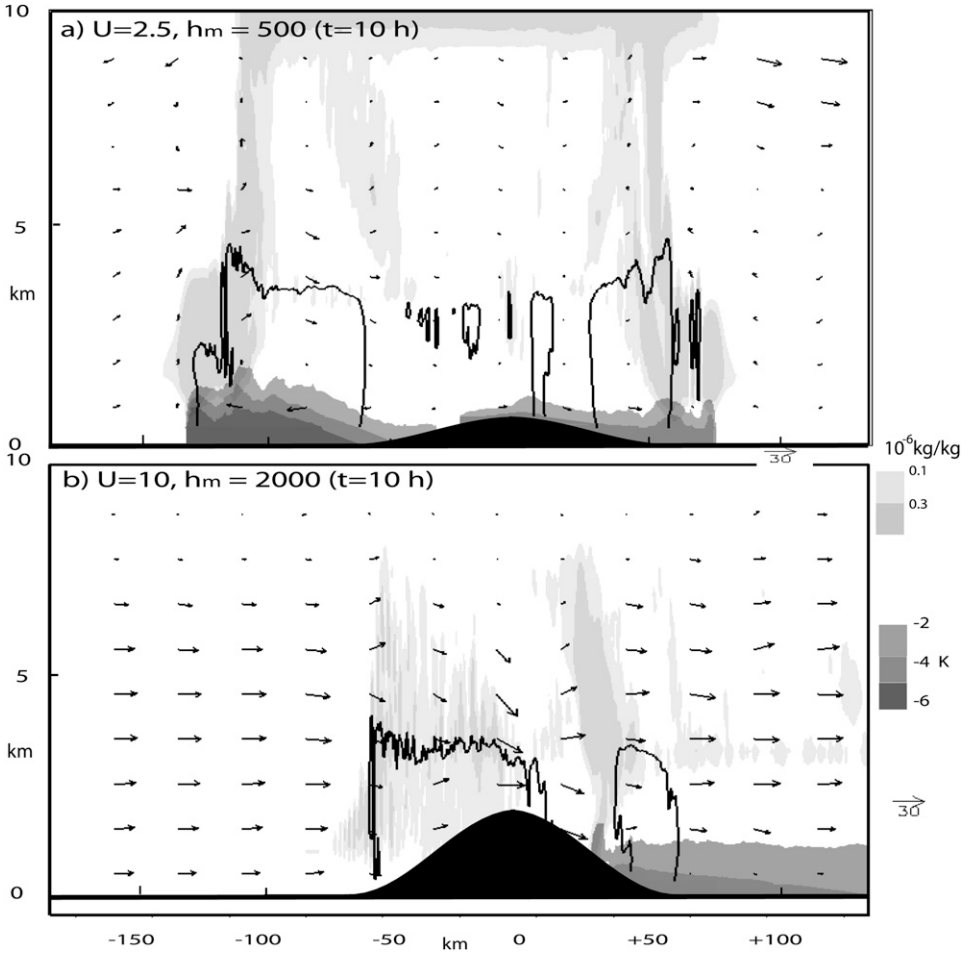

FIG. 9. As in Fig. 5, but for experiments with $a = 30$ km and (a) $U = 2.5$ m s^{-1} and $h_m = 500$ m and (b) $U = 10$ m s^{-1} and $h_m = 2000$ m. The two experiments correspond to the same value of h_mN/U.